UNIVERSITAT POLITECNICA DE CATALUNYA
Departament de Física i Enginyeria Nuclear

Second Harmonic Generation in Photonic Crystals

Jose Francisco Trull Silvestre

Memoria presentada para optar al grado de Doctor en Ciencias Físicas

Terrassa 1999

Chapter 4

Phase-matched second-harmonic generation in 3-D colloidal crystals

Since the beginning of the present decade, the use of photonic crystals to control the propagation of electromagnetic fields has been the subject of a large number of studies. Although most of the effort focused on the search of a material exhibiting a full photonic band gap in all directions in space, it has been recognized that systems exhibiting photonic band gaps in selected directions such as for example in one dimensional periodic systems may be of potential interest for studying a wide variety of phenomena. In particular, it has been showed in recent papers that nonlinear optical effects may play an important role in the development of more efficient optoelectronic devices whose properties are based on the existence of photonic band gaps in selected directions of space [Sca94]. Among the systems that have been shown to have photonic band gaps in the optical domain some of the more interesting are the 1-dimensional multilayer periodic structures and colloidal crystals. In fact, previous to the birth of the field of PBG, the use of birefringent sheared colloidal crystals for optical second-harmonic generation was already propsed by Lawandy et al. [Law88] after a macroscopic orientation of nonlinear molecules was observed in such crystals.

In previous chapters, attention was focused on the study of SHG from a single nonlinear monolayer into local modes of 1-dimensional photonic crystals with a defect, leading to he experimental observation of enhancement and inhibition of such radiation. In the present chapter we will continue the study of quadratic radiation by molecular monolayers, but when the nonlinear material is distributed periodically within the photonic crystal, instead of being limited to only a single layer. Because of this extended distribution of nonlinear material, efficient SHG requires fullfilment of the phase-matching condition. In our work we will show first how the nonlinear material can be introduced and distributed periodically within a photonic crystal and next, we will show how phase-matching can be achieved by using a mechanism based on the periodicity of the structure. This phase-matching mechanism, predicted independently by Bloembergen and Sievers [Blo70] and Yariv [Yar77], may be obtained in periodic structures due to the bending of the dispersion curve at the edges of the stop bands (or reflection bands)of the structure, which provides the necessary change in the effective refractive index close to these band edges.

Our results represent an experimental detailed study of a new mechanism of second-harmonic generation based on the constructive interference of light scattered by a periodic distribution of nonlinear material by means of this phase-matching process, which was proposed in a multilayer configuration [Mar94] or with the use of colloidal crystals [Mar97]. When radiation at a given frequency is incident upon one of these colloidal crystals, SH radiation is generated at each sphere due to the absence of inversion symmetry at the surface of each individual sphere forming the crystal mentioned. The phase-matching mechanism makes possible a coherent superposition of the resulting SH radiation by each sphere.On the other hand, an increase in the nonlinear susceptibility, $\chi^{(2)}$, of the material was obtained when each sphere was coated with molecules possessing a high second order susceptibility tensor different from zero such as Malachite Green.

This chapter will present a detailed study of this type of phase-matched second harmonic generation in colloidal crystals. In the first part of the chapter, after a brief review about colloidal structures, details on the experimental results of the study of the second harmonic light radiated by these kind of structures will be presented. In such experiments we fabricated several crystals of dye coated latex spheres with different concentrations. We performed measurements of the SHG by these crystals, that provided the necessary information to determine the surface character of the quadratic interaction as well as the intrinsic phase-matching mechanism responsible of the SH enhancement. A simplified model, based in surface SHG in a periodic structure will be presented in a second part, and in the last section of the chapter, a comparison between the experimental results and the theoretical model will be given.

Figure 4.1 shows the basic experiment configuration: when radiation at the fundamental frequency is incident on the crystal, SHG may be observed (Figure 4.1 (a)). The passive

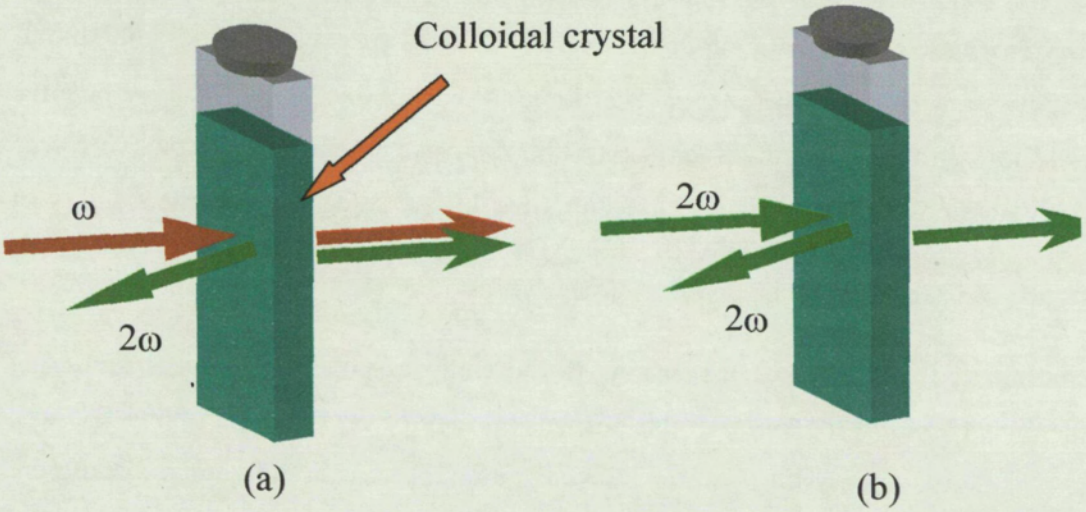

Figure 4.1

properties of the crystals are studied when radiation at the SH frequency is incident on the crystal (Figure 4.1 (b)).

1. Colloidal crystals

The word colloidal crystal is referred to any distribution of monodisperse colloids organized in a large-range ordered crystal [Pie83]. Typical size for individual colloids is about 0.1 μm to 10 μm, and the particular type of colloids may be very different. Several colloidal systems are found in nature such as precious opals and viruses. The possibility of disposing of synthetically prepared monodisperse colloids leads to ideal systems to study coherent scattering of visible light by arrays of single particles. These colloidal suspensions, whose individual particles consist of molecular agregates such as polystyrene or silica, are characterized by possessing functional charge groups at their surfaces which are susceptible of dissociation in highly polar solvents such as water, leaving each particle with a nonzero charge and a group of ions of the opposite sign in the solution. The resulting electrostatic interaction between the charged particles and the charged monovalent ions present in the solution are responsible for the formation of the colloidal suspension.

Throughout this work the colloidal suspension we will use is made of sulfate latex spheres. These spheres possess negatively charged sulfate groups terminating the polystyrene molecules in aqueous solution. The colloidal suspension is possible due to the repulsive force between spheres. This force is reduced by the presence of positive charged ions in the solution, which screen the repulsive interaction. Attractive forces due to Van der Waals interactions between molecules are responsible of the stability of the colloidal suspension.

The utility of these kind of suspensions in the study of coherent periodic scattering problems is based on the fact that this suspension may be crystallized, giving rise to a large-range ordered crystal. For the crystallization process to take place, different techniques have been proposed. The most commonly used is to remove positive ions from the solution by direct mixing of the suspension with an ionic exchange resin. The increase of the repulsive electrostatic force results in an ordered crystalline array of particles whose structural parameters depend on the density and size of the particles.

2. Experimental measurement of SHG in a 3-D colloidal crystal

2.1 Nonlinear colloidal crystal fabrication

For our study we will use a photonic crystal composed of polystyrene spherical particles of optical dimensions ordered in an unsheared lattice. SHG in the dipole approximation is allowed in these photonic crystals because of the local breaking of the inversion symmetry at the surface of each spherical particle [Mar97b][Bro69][Hei82]. In order to enhance the second order interaction in our experiments, we adsorbed a layer of strongly nonlinear molecules at the surface of each sphere in a colloidal crystal ordered in a face-centered cubic (fcc) lattice [Hil69][Wil74][Car84].

The surface of the spheres was coated with the nonlinear molecules by dialysis of stable aqueous suspensions of negatively charged microspheres with a positive charged chromophore of a dye molecule with high nonlinear coefficient. The negative surface charge of each sphere as well as the hydrophobic character of sulfate latex microspheres helps the formation of a surface of nonlinear molecules with a preferred orientation of the permanent dipole moment.

In our experiments we coated 0.115 μm diam spheres from Interfacial Dynamics Corporation with the chromophore part of the dye molecule. The polystyrene suspension was dialyzed overnight in a $2\cdot10^{-5}$ M aqueous solution of Malachite Green. The colloidal suspension of dye coated spheres was added to a high precision cell (50×10×1 mm) containing a mixed bed ion exchange resin in the bottom. After three or four days a single fcc crystal forms as stray ions in the solution diffuse to the resin.

Figure 4.2 shows an image of such a colloidal crystal in the experimental configuration, and schematically shows the dye coated spheres forming the colloidal crystal.

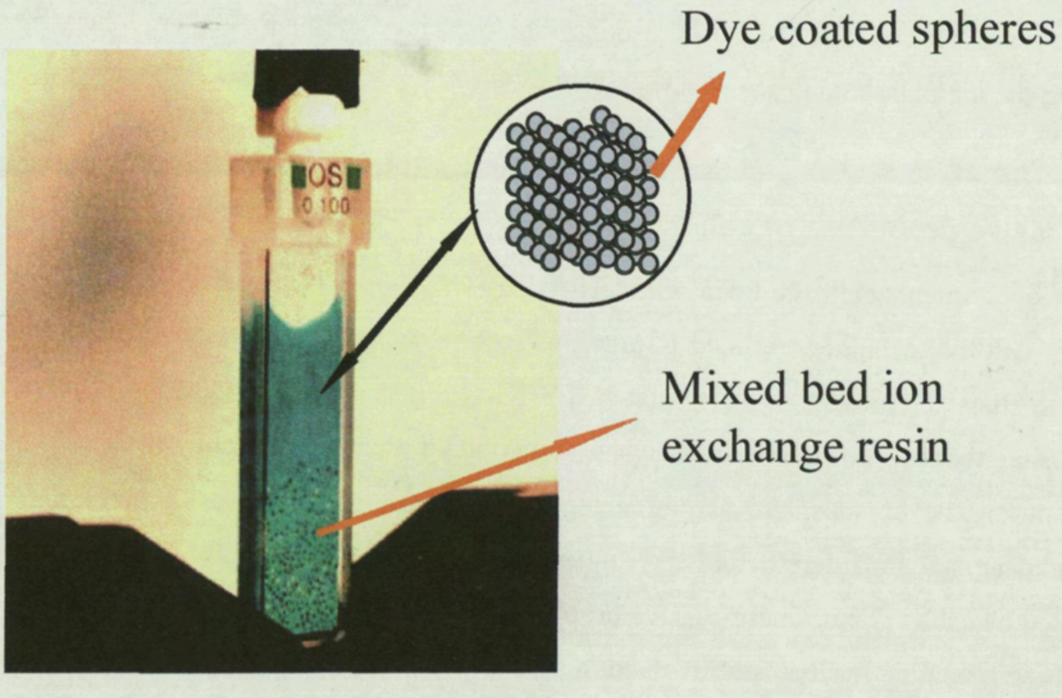

Figure 4.2 Colloidal crystal made of polystyrene spheres coated with the chromophore part of Malachite Green molecules. At the bottom of the cell is seen the mixed bed ion exchange resin, which induces the crystallization of the suspension.

In order to tune the Bragg reflection from the planes with indices of Miller (111) of the fcc lattice, the colloidal suspensions were concentrated in a dialysis membrane as indicated previously and diluted appropriately in distilled water before being added to the cell. In this way, we fabricated several fcc crystals with different lattice spacing using these suspensions of the same type of microspheres at different concentrations.

Each one of these crystals satisfies the Laue resonance condition

$$|\mathbf{G}| = 2|\mathbf{k}|\cos\theta \qquad 4.1.$$

for a given wavevector ***k*** of the second harmonic field at a different angle, θ, where θ is the angle between ***k*** and the reciprocal lattice vector ***G***, corresponding to the (111) planes. Since the wavelength of the SH light is fixed by the wavelength of the fundamental field, to move the resonance at a larger angle, one must change the modulus of the reciprocal lattice vector by decreasing the concentration of spheres. In this way we may change the Laue resonant angle of the crystal to higher values by diluting the initial colloidal suspension.

2.2 Passive properties of colloidal crystals

In our experiment, eight colloidal crystals made with dye coated latex spheres were grown with the technique outlined in previous section, with different concentrations in order to study the process of phase-matched SHG at different angular positions. Before measuring the SH generated light when radiation at the fundamental frequency is incident on the crystals, we should determine first the passive properties of each colloidal crystal in order to find the angle at which the Laue condition (Eq. 4.1) is satisfied by each crystal. These passive properties will help us to determine the origin of the phase-matching mechanism involved in the SHG process. The Bragg reflection band for each crystal is obtained by measuring the crystal reflectivity for incident radiation at the SH frequency (532 nm).

Figure 4.3 shows a schematic representation of the experimental setup used to measure the corresponding reflectivity of each crystal for incident light at the second-harmonic frequency 2ω. Light at 532 nm is obtained by doubling the frequency of a 35-ps Nd:YAG laser pulse at 1064 nm in potassium dihydrogen phosphate (KDP) crystal. The radiation at 532 nm is focused onto the crystal after being polarized in the TM direction (this polarization is chosen since the surface character of the quadratic nonlinear

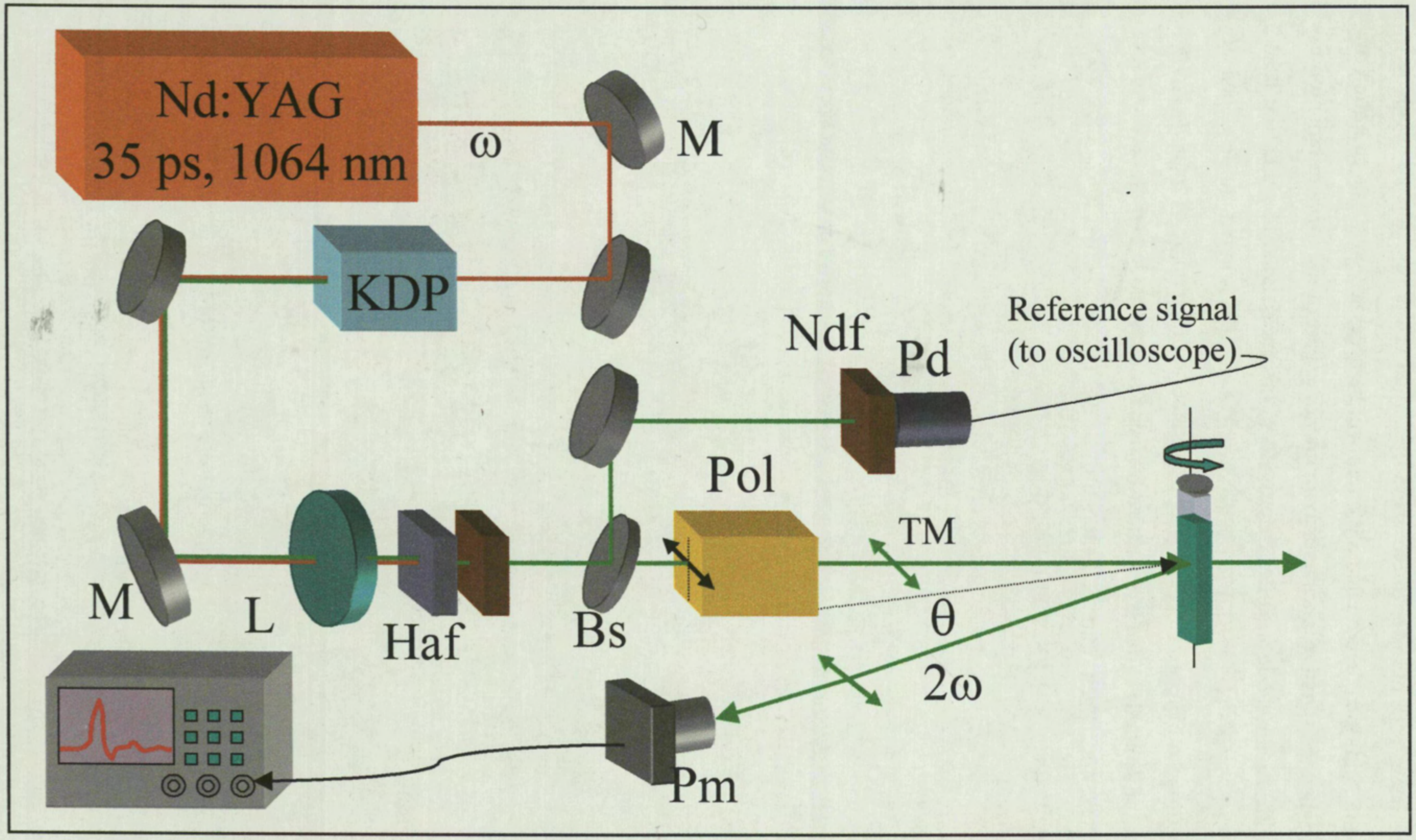

Figure 4.3 Experimental setup for the measurement of the Bragg reflection band of the colloidal crystal. The different elements are: M-mirror, L-converging lens, Pol-Glann-laser polarizer, Ndf- neutral density filters, Pm-photomultiplier, Pd-photodiode,Haf-heat absorption filter,Bs-beam splitter. The polarization state of the beams is TM.

radiation process will give as a result TM polarized SH radiation as will be made clearer later) using a Glann-laser polarizer. A heat absorption filter (Schott KG5) is placed in the beam path in order to eliminate the signal at the fundamental frequency from the beam. Additional neutral density filters will be necessary to avoid saturation of the detector when the signal reaches its maximum value. Part of the incident radiation is measured with a photodiode in order to provide a reference signal to check the laser stability at each pulse. The crystal is mounted on the same rotating stage described in chapter 2 in order to measure its reflectivity as a function of the angle of incidence. The reflected (or transmitted) signal is measured by using a photodiode and an oscilloscope Tektronix TDS540C. Each point is averaged over 100 pulses in order to overcome for the possible fluctuations in the laser pulse.

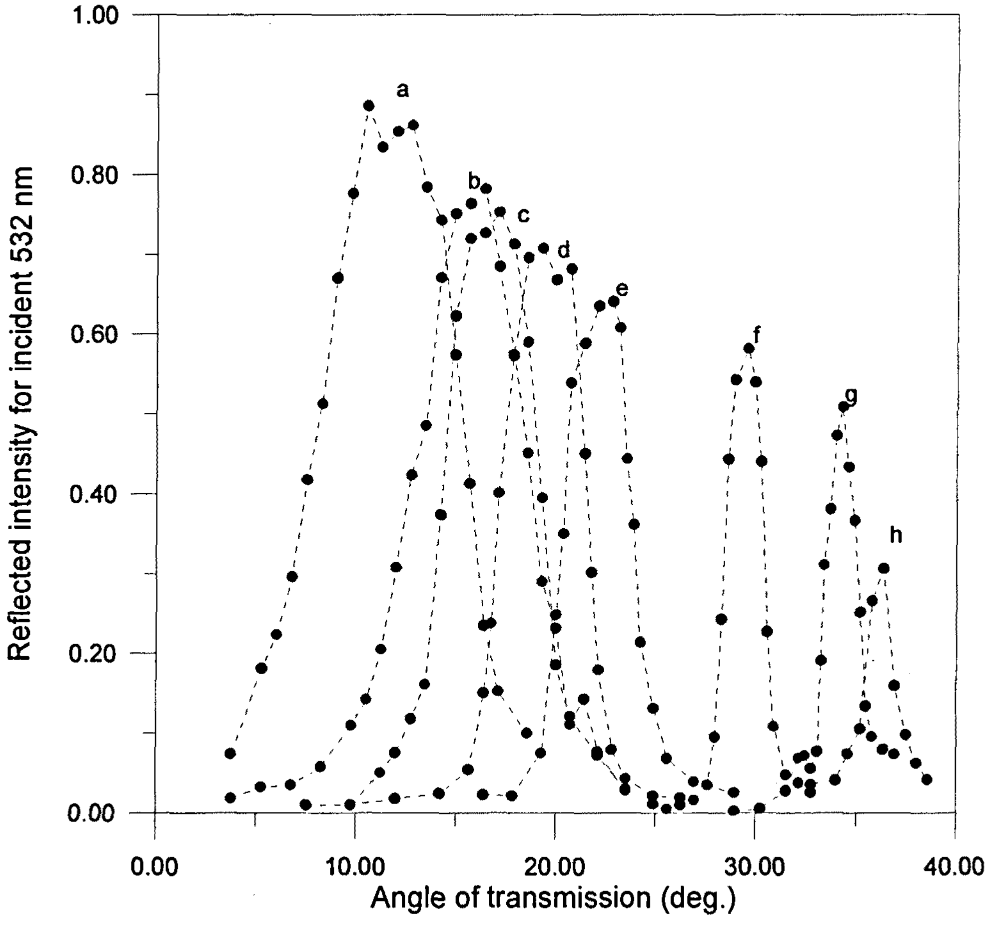

Figure 4.4 Reflection of incident light at 532 nm as a function of the the angle of the transmitted beam relative to the normal of the (111) planes from eight crystals with different lattice spacing. The circular dots correspond to the experimental values measured (the dashed curve is only a guide for the eye).

The measured reflectivity of each crystal is shown in Figure 4.4 for eight crystals with Laue resonances at the angles a) 12°, b) 15.5°, c) 16.7°, d) 19.5°, e) 22°, f) 29.7°, g) 34.3°, h) 36.2° where the first crystal corresponds to the colloidal suspension without additional water and the last crystal is diluted at 40 % in distilled water. In order to correlate all the curves a measurement of the incident intensity was performed in each case. In Figure 4.4 all the curves have been normalized to the reflectivity at the angle satisfying the Bragg condition for the crystal with higher reflectivity. A measurement of the reflected SH light when the cell is filled with water was also performed. The given data in Figure 4.4 have been already corrected from this factor in order to account solely for the crystal reflectivity.

It can be shown from Figure 4.4 how each one of the crystals posses a Bragg reflection curve at a different angular position. This Bragg reflection band is moved towards higher angles as the concentration of spheres becomes smaller. The width of the gap is reduced as the Laue condition is satisfied at larger angles, as may also be seen in Figure 4.4. Notice that the angle appearing in this and next figures is not the incident angle of the radiation in air, θ_{inc}, but the angle of refraction, θ, determined after applying Snell's law between air and water (n=1.33).

2.3 SHG in colloidal crystals

Once the Bragg reflection bands for each one of the crystals has been measured, next step will be the measurement of the SH reflected light from the colloidal crystals for incident light at the fundamental frequency. SHG is possible, in the dipole approximation, in these crystals because of the local breaking of the inversion symmetry at the surface of each spherical surface [Mar97]. When a beam at the fundamental frequency is incident upon each individual sphere, SHG is generated at any given portion of the sphere surface. The constructive interference of the SH light scattered from the sphere results in a nonvanishing radiation at the SH frequency. The surface nonlinear susceptibility is enhanced by a factor of 10 due to the presence of the dye coating each sphere.

The coherent superposition of the SH energy radiated by each sphere results in a SH radiated beam at a given direction in space. The phase-matching mechanism between the fundamental and SH beams necessary for a continuous growth of the SH intensity is provided by the bending of the dispersion curve at the boundary of the forbidden zone or Bragg reflection band. Since each crystal has a different lattice constant, it is expected that the resulting SH beam appears at different angle for each crystal.

The measurement was performed using the experimental setup outlined in Figure 4.5. Now the KDP crystal has been removed and the fundamental beam at the wavelength of 1064 nm is incident on the crystal after being passed through neutral density filters in order to avoid saturation at the detector for the highest values of the measured intensity. A Glann-laser polarizer sets the desired polarization of the beam. The reflected (or transmitted) intensity is measured with a photomultiplier after passing a heat absorbing filter and interference filter at 532 nm. Each pulse is averaged over 100 pulses in order to take account for possible fluctuations in the laser beam. Although the SH intensity may be measured either in a reflection or transmission geometry, a reflection geometry is chosen, since interference with the SH light generated in the bulk of the cell is strongly reduced in this case.

The results of the SH radiated intensity of each crystal are shown in Figure 4.6 as a function of the transmission angle. It can be seen that when the Laue condition is satisfied close to the normal incidence, generation of SH is comparatively very small. The efficiency of the SHG process increases up to a certain angle, to decrease later when the resonance condition is satisfied at larger angles. Note that SHG as a function of the angle of incidence in such colloidal crystals exhibits the bell-shaped curve that is expected from generation at the interface between two materials that exhibit inversion symmetry in the bulk [Hol90]. The surface character of this type of SHG is further confirmed by the fullfilment of the polarization selection rule for surface SHG from a nonlinear monolayer with $C_{\infty v}$ symmetry [Heinz]. When the fundamental field is polarized parallel to the plane of incidence (TM polarized), only the SH field polarized in the same direction should be nonzero, as confirmed by an experimental measurement of an intensity 500 times larger for this polarization than for the perpendicular one. When the fundamental field is polarized in the perpendicular direction with respect to the plane of incidence, the SH field in this direction should vanish, as confirmed by the experimental measurement of an intensity more than one order of magnitude larger in the direction parallel to the plane of incidence.

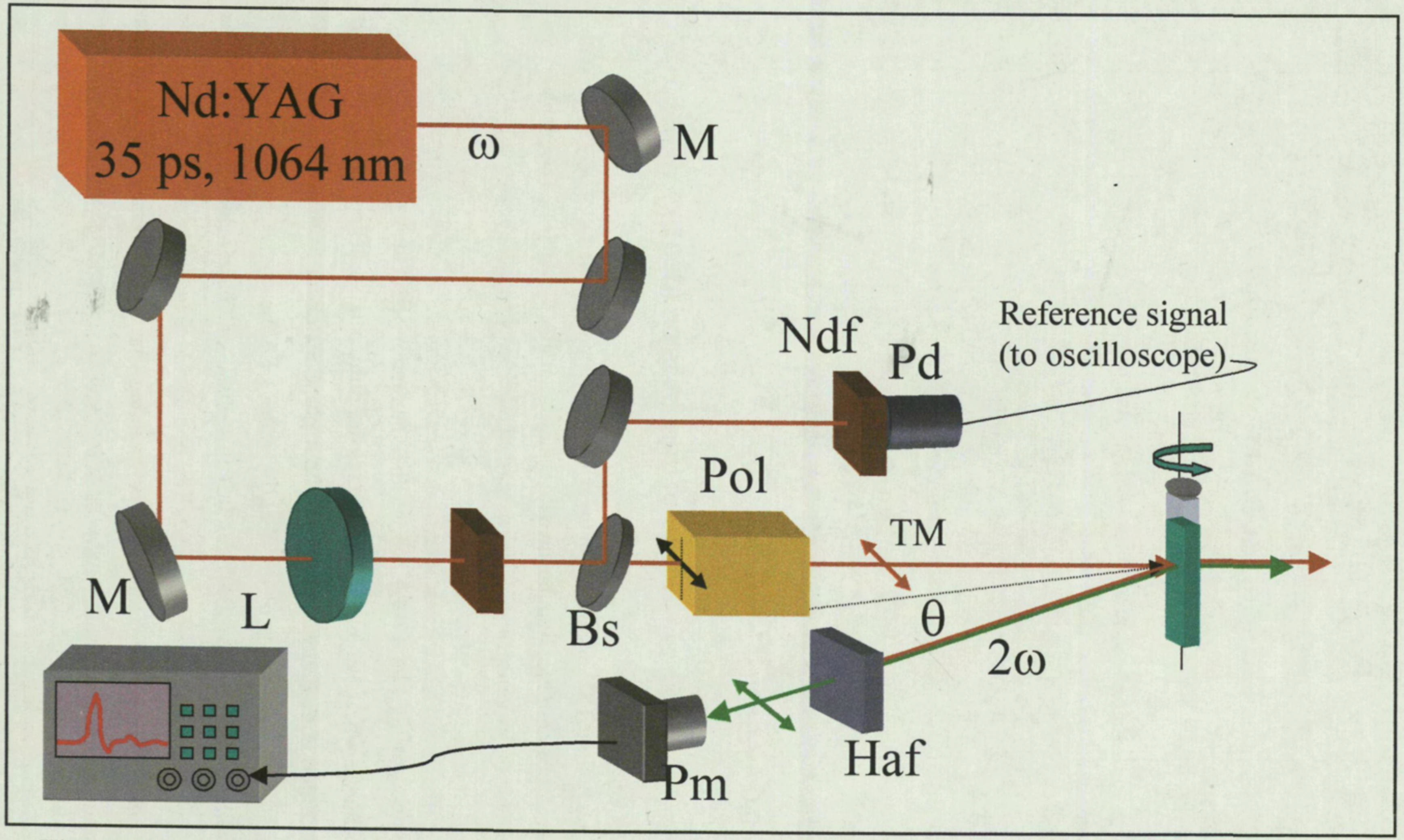

Figure 4.5 Experimental setup for the measurement of the SHG by the colloidal crystal.
The different elements are: M-mirror, L-converging lens, Pol-Glann-laser polarizer, Ndf- neutral density filters, Pm-photomultiplier, Pd-photodiode,Haf-heat absorption filter,Bs-beam splitter. The polarization state of the beams is TM.

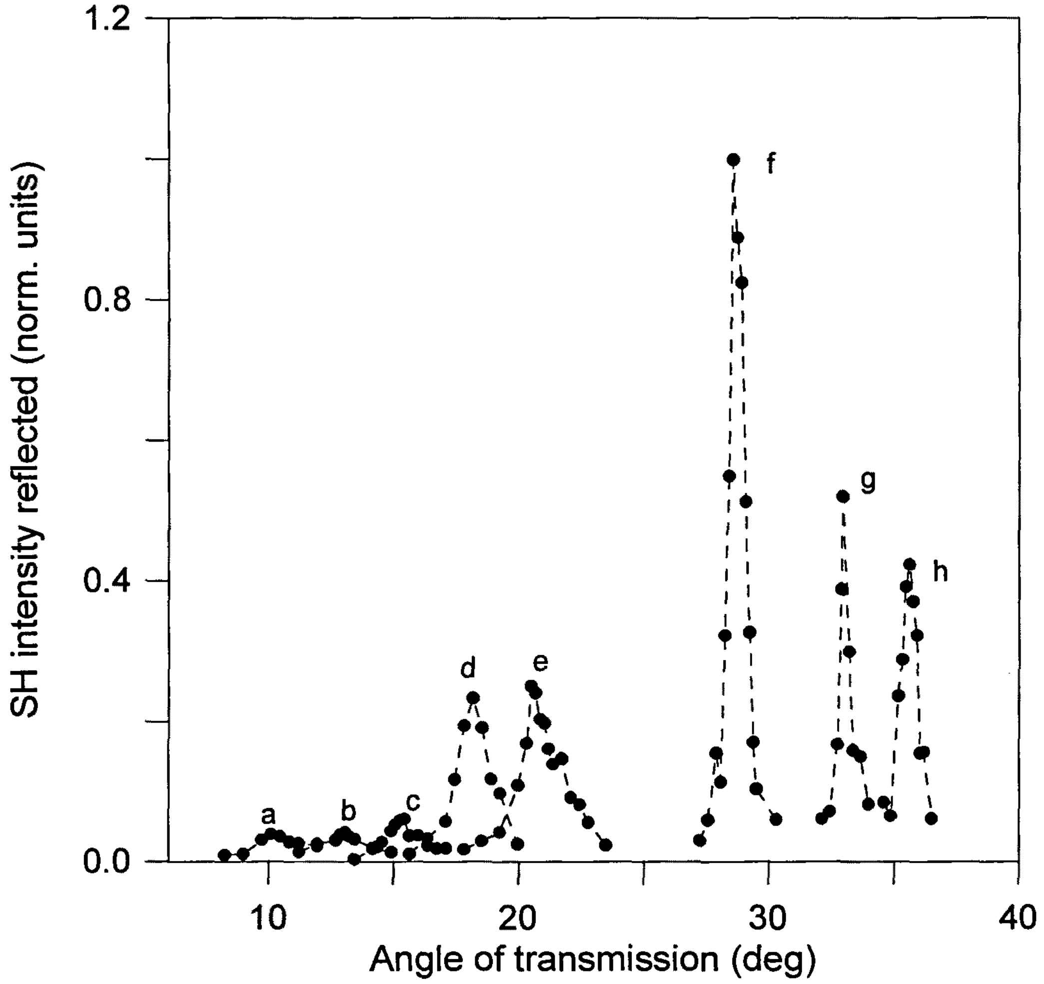

Figure 4.6 Reflected SH intensity from the same eight crystals in Figure 4.4. as a function of the angle of the transmitted beam relative to the normal of the (111) planes. The circular dots correspond to the experiemental points (the dashed line is only a guide for the eye).

Notice by comparing Figures 4.4 and 4.6 that maximum SH is always generated at the smaller angle side of the corresponding crystal stop band or Bragg reflection band shown in Figure 4.4. This is consistent with a phase-matching of the fundamental and SH beams due to a decrease of the effective index of refraction at the left edge of the Bragg reflection curve. One also sees that this phase-matching resonance broadens as the concentration of spheres increases, as one would expect by an increase in the number of scattering sites and defects breaking the phase relation between the fundamental and SH beams.

2.4 Second harmonic generation efficiency

As is well known, second harmonic conversion efficiency is proportional to the square of the length of the crystal used. However, in a nonperfect crystal, actual power conversion is limited by the scattering losses due to the presence of defects in the crystal lattice, the dispersion in the sphere diameter and the non-negligible absorption cross-section of Malachite-Green.

In the nonlinear colloidal crystals of our work, the power conversion efficiency from the fundamental to the SH field may be readily determined from the experimental measurements reported in the previous chapter. An accurate estimation of the converted power may be obtained by considering the specific characteristics of the photomultiplier and of the filters used in the experimental setup. For the crystal with maximum SHG (Figure 4.6 (f)) we found a power conversion efficiency:

$$\eta = \frac{P^r_{2\omega}}{P_\omega(0)} \cdot 100 = 10^{-12}\%$$

where $P^r_{2\omega}$ is the reflected SH power and $P_\omega(0)$ is the incident power at the fundamental frequency. Note that this low value of power efficiency is in part due to the several loss mechanisms present in the crystals, as commented in the preceeding paragraph, which limit the effective length of the crystal contributing to the SHG process and consequently, reduces the amount of nonlinear material contributing to the growth of the signal.

In order to evaluate the limitations imposed by the losses in the SHG process, we will include in the theoretical model an effective absorption coefficient that is defined through the relation:

$$T(L) = T(0)\exp(-\alpha L) \qquad 4.2.$$

where $T(L)$ is the value of the transmitted intensity at length L and $T(0)$ is the incident intensity on the crystal. For these crystals a power conversion will be approximately proportional to $L^2 exp(-\alpha L)$.

An experimental value of the absorption coefficient of each one of the crystals may be obtained by measuring the transmitted intensity of each one of the crystals at normal incidence, far from any Bragg resonance, and the intensity incident on the crystal, as may be seen in Eq. 4.2. Additional measurements of the same parameters for a given cell without crystal were also performed in order to take into account the loses introduced by the presence of the cell. These measurements were taken at the wavelengths of the fundamental beam (1064 nm) and also for incident radiation at the SH frequency (532 nm). The experimental setup for the measurements of the absorption coefficient is shown schematically in Figure 4.7. A beam at the fundamental wavelength of 1064 nm, provided by the Nd:YAG laser is incident upon the crystal at normal incidence and the transmitted intensity is measured with a photodiode and monitored through an oscilloscope. The incident intensity is obtained by removing the crystal from the beam path. Neutral density filters were used in order to avoid saturation of the detector. Each experimental measurement was averaged over 60 pulses in order to account for the possible fluctuations in the incident beam. A KDP crystal provides radiation at the SH frequency in order to measure the absorption coefficient at the wavelength of 532 nm. In this case a heat absorption filter was used in order to eliminate the signal at the fundamental frequency from the beam path. The measurement takes place in the same way as indicated for the fundamental case.

The results of the measurements of the absorption coefficients for the eight crystals used are shown in Figure 4.8 for both wavelengths. It may be seen from these measurements that the absorption coefficient at the fundamental frequency is approximately constant for all the crystals, with an average value of 5 cm^{-1}, while for the SH frequency it is observed that the absorption coefficient increases as the crystal concentration increases, with values ranging from 45 cm^{-1} for the crystal with the lowest concentration of spheres up to 60 cm^{-1} for the crystals with the largest concentration of spheres. These values will be used later in a comparison between experimental and theoretical results.

In order to give an estimation of the enhancement that can be achieved in the SHG by optimizing the process of crystal fabrication we shall consider the different aspects that contribute to an enhancement of the SHG efficiency. On one hand, the concentration of Malachite Green molecules used in the crystal fabrication was of the order of 10^{16} molecules/cm^3 which gives an average value of 125 molecules adsorbed at each sphere

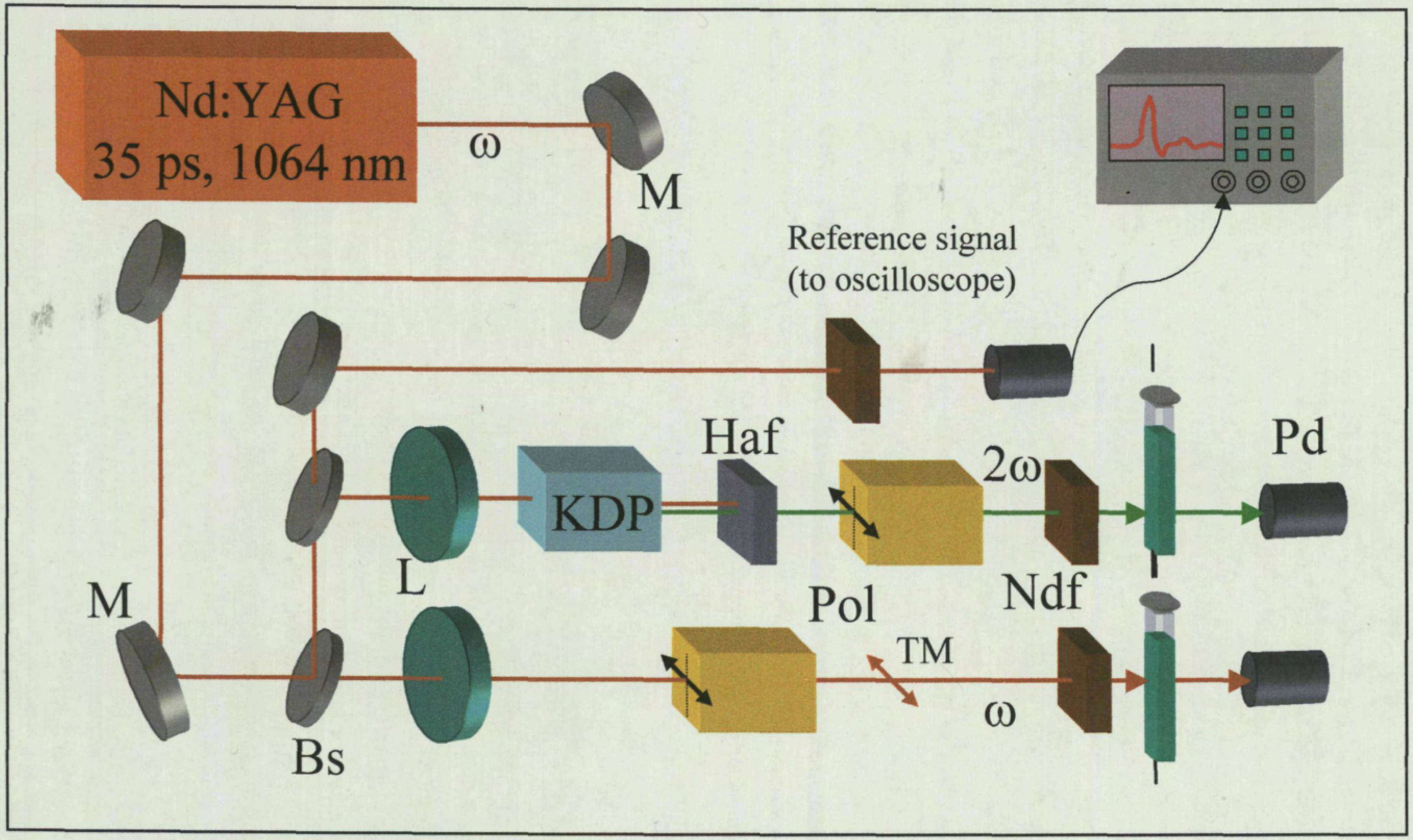

Figure 4.7 Experimental setup for the measurement of the absorption coeffoicient of the colloidal crystal for the fundamental and SH wavelengths.The different elements are: M-mirror, L-converging lens, Pol-Glann-laser polarizer, Ndf- neutral density filters, Pd-photodiode,Haf-heat absorption filter,Bs-beam splitter. The polarization state of the beams is TM.

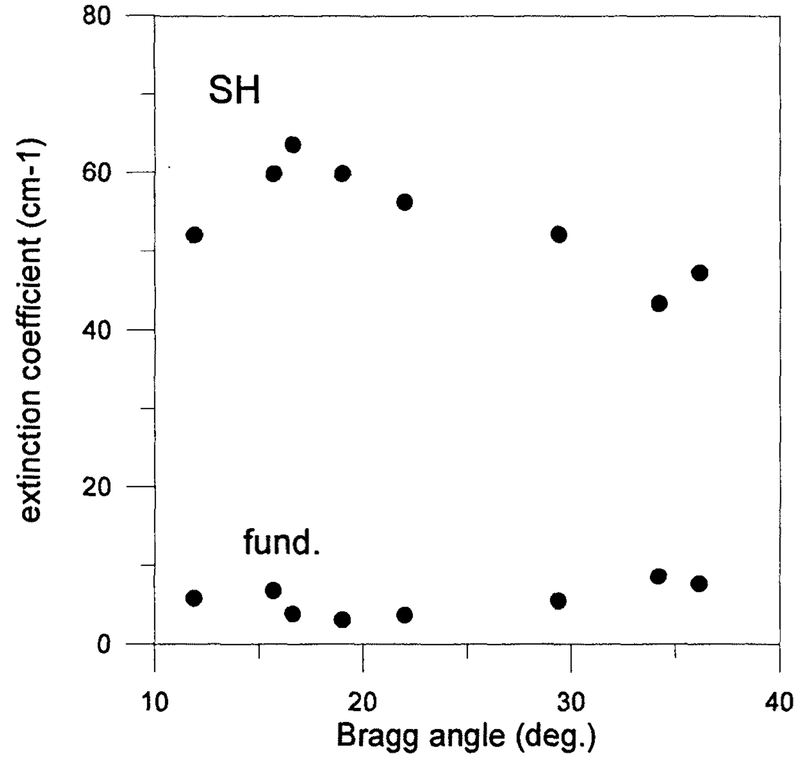

Figure 4.8 Absorption coefficient for the same eight crystals of Figures 4.4 and 4.6 for incident radiation at the fundamental wavelength (1064 nm) and at the SH wavelength (532 nm).

of the colloidal crystal (for the crystal in Figure 4.6 (f) the spheres concentration is of the order of $8{\cdot}10^{13}$ spheres/cm^3). The number of molecules adsorbed at the surface of the spheres can be increased by a factor of 300, and still the crystal should be able to crystallize, so an increase of the order of 10^5 in the radiated SH power could be achieved by increasing the concentration of the nonlinear molecules. On the other hand, we will see in section 3 that the values of the absorption coefficients measured for these crystals results in a saturation of the SH signal after 2500 layers. If the losses of the crystals are reduced, improving the quality of such crystals, a quadratic growth of the SH signal will be achieved. From Figure 4.16 we can estimate that only the first 200 layers of the crystal (corresponding to a crystal length of approximately 0.05 mm), contribute to a quadratic growth of the signal, which tends to saturate as the number of layers is increased. For a crystal with negligible absorption over a length of 1 cm the SHG power could be enhanced by a factor of $4{\cdot}10^4$. An additional enhancement can be obtained by selecting the nonlinear molecules in order to increase the resulting nonlinearity. The choice of different molecules does not affect the phase-matching process which is related to the periodicity of the structure. By increasing the nonlinearity 10 times, an enhancement of 100 in the SH power is obtained. From these estimations we see that an enhancement of the order of 10^{12} could then in principle be obtained by the suitable improvement of the several factors mentioned.

3. Analysis of SHG in colloidal crystals

In order to explain the observed second order nonlinear process we should develop a convenient model to treat this type of interaction. A first approach to model the nonlinear interaction should be to consider the scattered SH light from a given sphere of material coated by a nonlinear monolayer and then account for the cooperative scattering from all the spheres located on a plane normal to the direction of propagation of the incoming fundamental beam. It was demonstrated [Mar97b], by solving Maxwell's equations with a nonlinear source term in the Rayleigh-Gans approximation, that a given coated dielectric sphere may lead to a nonvanishing field at the SH frequency. However, when the cooperative scattering from all the spheres is taken into account, the Rayleigh-Gans approximation leads to results only partially in agreement with experimental results. Presumably, an accurate description would be provided by the Mie scattering theory consisting of an exact solution of the Maxwell equations in a structure composed of nonlinear spherical particles ordered in a 3D lattice.

In order to provide an alternative approach to the problem using a model of manageable proportions and that accounts for the essential features of the SHG process observed, we developed a theoretical analysis based on the use of plane layers that includes both the surface character of the nonlinear process and the periodicity of the dielectric structure that provides the phase-matching mechanism. We assimilated each of the (111) planes of the fcc lattice by a plane slab of dielectric material that is coated on both sides by a monolayer of nonlinear molecules as shown schematically in Figure 4.9. Each plane of spheres is replaced by a dielectric material of thickness D', slightly smaller than the diameter of the sphere and with an effective index of refraction n_l, and the molecules coating the surface are replaced by the front and back nonlinear layers. These nonlinear bilayers are separated by a dielectric slab of thickness s and refractive index n_o, which is assumed to be that of water. Figure 4.10 shows a section of three of such bilayers

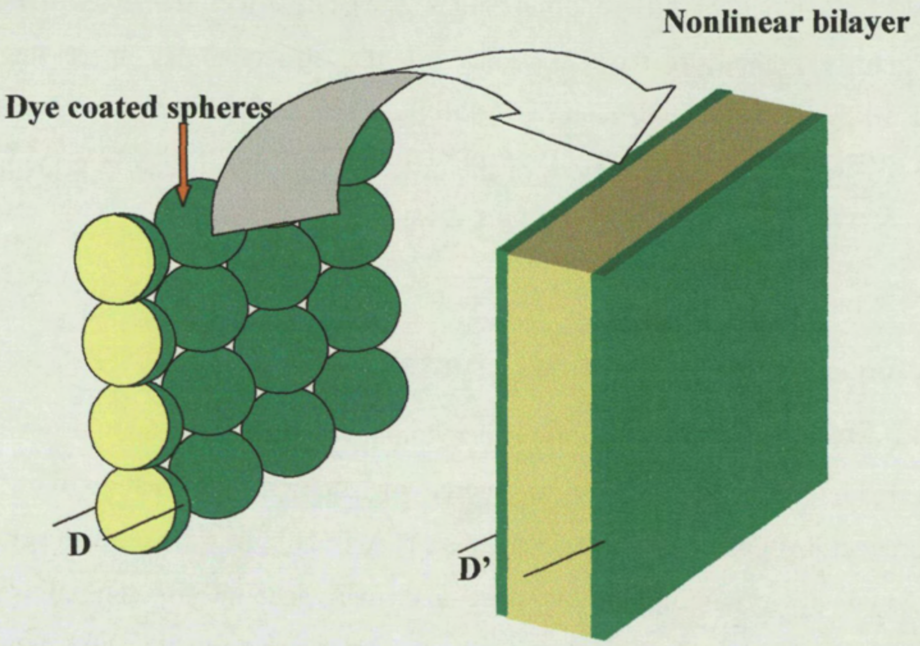

Figure 4.9 Schematic representation of the bilayer model used to simulate the process of quadratic nonlinear radiation by colloidal crystals made of dye coated latex spheres. The thickness of the bilayer replacing the plane of spheres is not necessarily the same as the spheres diameter.

together with its main geometrical parameters. Note that the effective index of refraction and thickness of the bilayers will not correspond in general to the real values of the index of refraction and thickness of the spheres, and will become parameters to be adjusted in order to simulate the real nonlinear quadratic process.

Note that this planar model based on planar structures enhances contribution from molecules located on a portion of the sphere surface that is close to the normal with respect to the surface of the cell, or, in other words the molecules located at the front and back of the spheres. On the other hand, this planar structure suppresses contribution from molecules located on a portion of the sphere surface that is normal to the plane containing the spheres or, in other words, the side molecules. This is in agreement with what occurs in the real crystal, since this last group of molecules has in the spherical geometry a smaller contribution because its contribution to SHG is canceled by molecules located on the opposite side of the sphere. In order to preserve the all-possible orientations of the molecular nonlinear dipoles on the original plane of spheres, we assumed a structure where the dipole planes belong to the $C_{\infty v}$ symmetry group. The

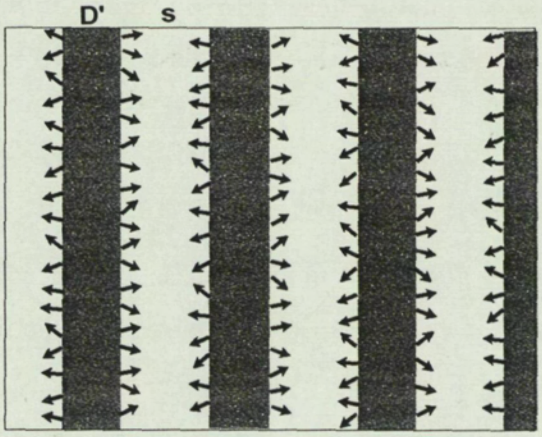

Figure 4.10 Section of three bilayers of the periodic structure considered in the theoretical analysis. The index of the dark layers where the NL molecules are adsorbed is n_1, and the index of the surrounding material is n_o.

dipole projection along the symmetry axis of each plane has opposite directions in each side of the dielectric slab.

At this point, generation of SH light at each bilayer may be easily determined by the transfer matrix method applied to nonlinear interactions that is explained in detail in chapter 2. The equation to be solved is the linear equation with a nonlinear source term (Equation 2.20)

$$\nabla \times (\nabla \times \mathbf{E}_{2\omega}) - \frac{n_{2\omega}^2 (2\omega)^2}{c^2} \mathbf{E}_{2\omega} = \mu_o (2\omega)^2 \mathbf{P}_{NL}^{2\omega} \qquad 4.3.$$

where the nonlinear source term $\boldsymbol{P}_{NL}$ is only nonvanishing inside each nonlinear layer, $n_{2\omega}$ is the refractive index at the SH frequency in the medium considered, and $\boldsymbol{E}_{2\omega}$ is the solution for the field at the SH frequency, written as a superposition of plane waves oscillating at the frequency 2ω. In solving Equation 4.3, we consider, as in chapter 2, that the transfer of energy from the fundamental to the SH beam occurs only in the direction of the incident fundamental beam. This approximation is well justified, since the solution of the wave equation at frequency ω in a periodic structure with a Bragg resonance at 2ω indicates that, when the values of the effective refractive index measured in our experiment are used, the forward-propagating field amplitude for the fundamental field is ten times larger than the corresponding backward-propagating component. Then, the radiated field intensity at 2ω by the forward propagating fundamental field is one hundred times higher than the backward propagating second harmonic field.

An exact analytical solution of Equation 4.3 can be found in the nonlinear bilayer slab when the thickness of each nonlinear monolayer is small compared with the wavelength, which obviously is the case. In each nonlinear layer the field is written as a superposition of a forward and a backward propagating plane wave solution of the homogeneous part of Eq. 4.3 and a source term corresponding to the particular solution to the same equation. By establishing appropriate boundary conditions at each interface of the nonlinear layers with the corresponding dielectric slab, one can connect the solution within the nonlinear layer with the fields in the dielectric slabs given by the superposition of a forward and a backward propagating plane wave solution of the homogeneous part of Eq. 4.3. At this point, by means of the simple matrix sum and multiplication technique showed in chapter 2, one can determine the reflected and transmitted fields into the slab of index n_o surrounding each nonlinear bilayer slab, given in terms of the incident fundamental and SH fields. Full information on the reflected fields of the periodic structure needed in this calculation is provided by these input fields.

The relation between the fields at consecutive slabs of index n_o may be written in matrix form as

$$\begin{pmatrix} E_+^o(n-1) \\ E_-^o(n-1) \end{pmatrix} = \begin{pmatrix} AE & BE \\ CE & DE \end{pmatrix} \cdot \begin{pmatrix} AF & BF \\ CF & DF \end{pmatrix} \cdot \begin{pmatrix} E_+^o(n) \\ E_-^o(n) \end{pmatrix} + \begin{pmatrix} SA \\ SB \end{pmatrix} \qquad 4.4.$$

where $E_\pm^o(n-1)$ and $E_\pm^o(n)$ denote the forward (+) and backward (-) propagating field components in the dielectric slab of index n_o at the front and at the back of the n^th^ nonlinear bilayer respectively. The different terms of the expression are given by

$$\begin{pmatrix} SA \\ SB \end{pmatrix} = \begin{pmatrix} AE & BE \\ CE & DE \end{pmatrix} \cdot \begin{pmatrix} E_{NL}^{1+} \\ E_{NL}^{1-} \end{pmatrix} + \begin{pmatrix} E_{NL}^{2+} \\ E_{NL}^{2-} \end{pmatrix} \qquad 4.5.$$

where

$$AE = DE^{*} = \frac{1}{2}\left(\frac{\cos\theta_1}{\cos\theta_o} + \frac{n_1}{n_o}\right)\exp i\left(k_{1z} - k_{oz}\right)s$$

$$BE = CE^{*} = \frac{1}{2}\left(\frac{\cos\theta_1}{\cos\theta_o} - \frac{n_1}{n_o}\right)\exp - i\left(k_{1z} + k_{oz}\right)s$$

and

$$AF = DF^{*} = \frac{1}{2}\left(\frac{\cos\theta_o}{\cos\theta_1} + \frac{n_o}{n_1}\right)\exp - ik_{1z}(D+s)$$

$$BF = CF^{*} = \frac{1}{2}\left(\frac{\cos\theta_o}{\cos\theta_1} - \frac{n_o}{n_1}\right)\exp - ik_{1z}(D+s)$$

The nonlinear source terms appearing in Eq. 4.5. are given by:

$$E_{NL}^{1\pm} = \frac{i\omega}{\varepsilon_o c}\left(\mp\frac{P_{NLx}}{n_o^{2\omega}} + \frac{P_{NLz} n_1^{\omega} sin\theta_{1\omega}}{(n_1^{2\omega})^2 \cos\theta_o}\right)\exp i(k_{s1z} \mp k_{oz})s$$

$$E_{NL}^{2\pm} = \frac{i\omega}{\varepsilon_o c}\left(\mp\frac{P_{NLx}}{n_1^{2\omega}} - \frac{P_{NLz} n_1^{\omega} sin\theta_{1\omega}}{(n_1^{2\omega})^2 \cos\theta_1}\right)\exp i(k_{s1z} \mp k_{1z})(D+s)$$

where n_i^{ω} and $n_i^{2\omega}$ are the refraction indices at the fundamental and SH frequency respectively in medium i (i=0,1), θ_i are the angles of propagation with respect to the normal to the slabs at the SH frequency in medium i, $\theta_{i\omega}$ are the corresponding propagation angles in medium i for the field at the fundamental frequency and the wavevectors are defined as

$$k_{iz} = \frac{n_i^{2\omega} 2\omega}{c}\cos\theta_i \qquad \text{and} \qquad k_{siz} = \frac{n_i^{\omega} 2\omega}{c}\cos\theta_{i\omega} \quad \text{(i=0,1)}$$

Note that in the present case we have two source terms corresponding to the front and back nonlinear layers of the dielectric slab, for which the P_{NLz} term has opposite sign. The nonlinear source terms P_{NLz} and P_{NLx} are determined after contraction of the nonlinear susceptibility, expressed in terms of its effective surface nonlinear susceptibility components and of the tensor E_ω^2 solution of the homogeneous wave equation at the frequency of the fundamental wave.

Now, the SH intensity reflected or transmitted by the whole periodic structure is easily obtained by multiplication of the matrices corresponding to the consecutive slabs. The relation between the fields in the first and last layers with refractive index n_o is written as

$$\begin{pmatrix} E_+^o(0) \\ E_-^o(0) \end{pmatrix} = \begin{pmatrix} A & B \\ C & D \end{pmatrix} \cdot \begin{pmatrix} E_+^o(N) \\ E_-^o(N) \end{pmatrix} + \begin{pmatrix} A_{NL} \\ B_{NL} \end{pmatrix} \qquad 4.6.$$

with

$$\begin{pmatrix} A & B \\ C & D \end{pmatrix} = \left[\begin{pmatrix} AE & BE \\ CE & DE \end{pmatrix} \cdot \begin{pmatrix} AF & BF \\ CF & DF \end{pmatrix} \right]^N$$

$$\begin{pmatrix} A_{NL} \\ B_{NL} \end{pmatrix} = \sum_{n=0}^{N-1} \left[\begin{pmatrix} AE & BE \\ CE & DE \end{pmatrix} \cdot \begin{pmatrix} AF & BF \\ CF & DF \end{pmatrix} \right]^n \begin{pmatrix} SA \\ SB \end{pmatrix}$$

Now, applying the boundary condition that no SH field is incident from the left or the right side of the whole structure, and the fundamental is only incident from the left, the reflected and transmitted SH intensity is given by

$$R_{SH} = \left| B_{NL} - \frac{C}{A} A_{NL} \right|^2 \qquad \text{and} \qquad T_{SH} = \left| - \frac{A_{NL}}{A} \right|^2 \qquad 4.7.$$

With these equations we can calculate now the SH generated by a given structure made of N nonlinear bilayers of this kind.

Figure 4.11 shows an schematic diagram of the fields present at one of the bilayers, where $E_\pm^o(n-1)$ and $E_\pm^o(n)$ are the fields at the front and back of the n$^{\text{th}}$ nonlinear bilayer as seen previously, $E_\pm^d$ corresponds to the field components inside the bilayer, $E_\pm^{nli}$ are the field components of the homogenous solution at the slabs and E_+^{si} are the fields given by the particular solutions at each slab.

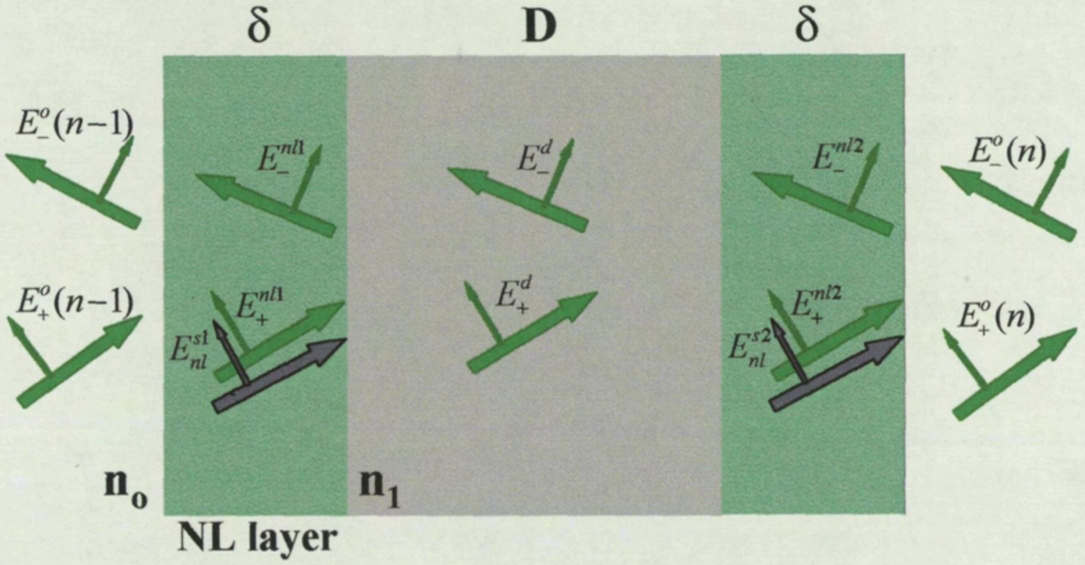

Figure 4.11 Schematic representation of the fields at the SH frequency in one of the bilayers. The different components of the fields have been described in the text.

Once the principal characteristics of the model have been established, the following step is to see if the generation of SH by a structure made of nonlinear bilayers exhibits the main characteristics found in the experimental measurements, i.e. surface character of the quadratic nonlinear radiation and phase-matching mechanism.

To explain the phase-matching mechanism we will consider two structures with the same bilayer thickness, *D*, i.e. with the same sphere size but with different spacing between bilayers, *s*. In this way the concentration of bilayers is reduced as the distance *s* is increased so we can move the Bragg reflection band of the given structure to higher angles by increasing *s*. Figure 4.12 shows the SH intensity reflected by the bilayer structure which presents a Bragg curve centered at 16 degrees for increasing number of bilayers. The different reflectivity curves correspond to the given structure with a number of layers given by: a) 1, b) 5, c) 10, d) 20, e) 50, f) 100. Note that the SH intensity reflected for 1 bilayer (Figure 4.12 (a)) shows the bell shaped form typical of surface SH phenomena. It may be observed how the initial bell-shaped curve becomes a sharp resonance as the number of layers is increased. The position of such resonance is

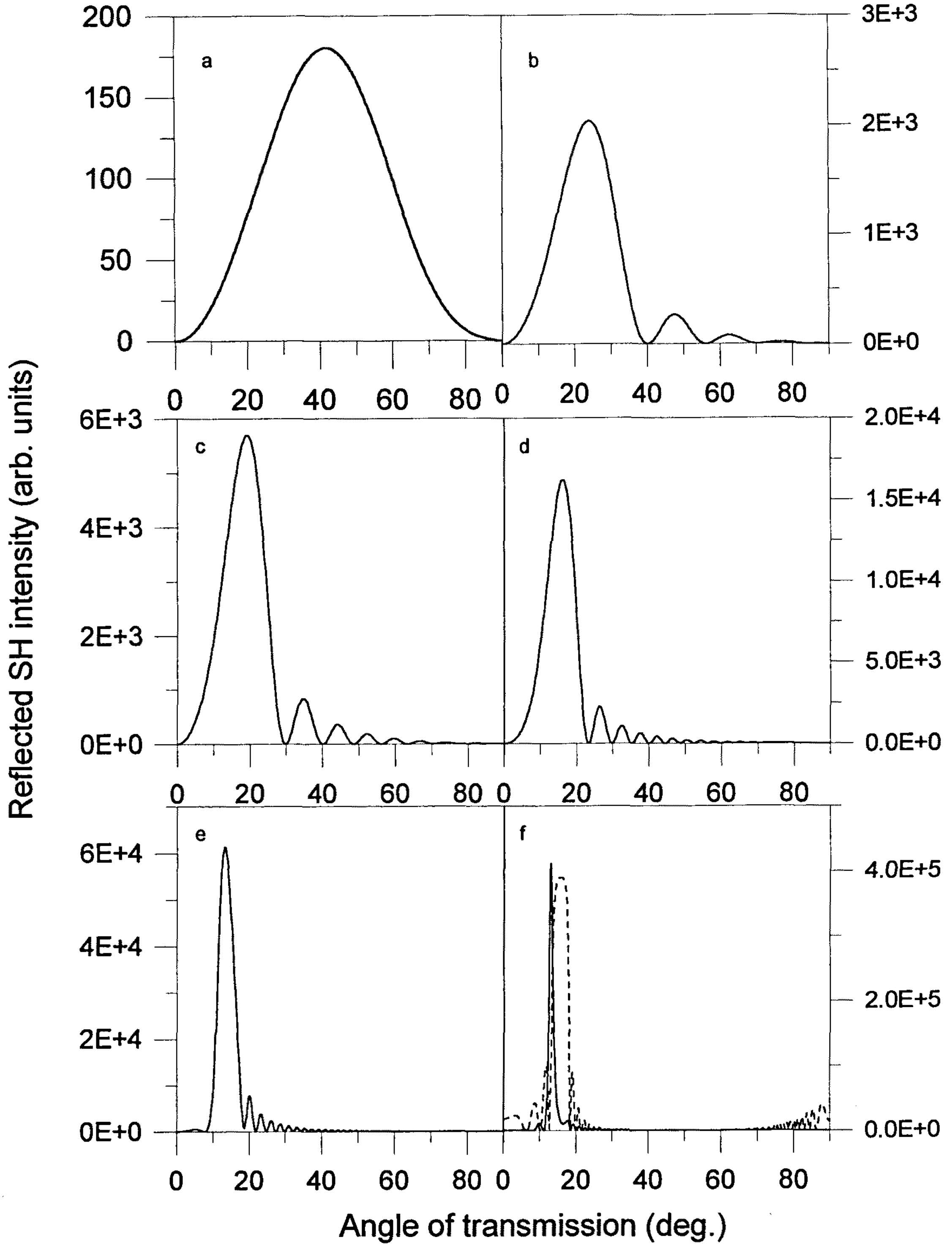

Figure 4.12 Reflected SH intensity as a function of the transmission angle for a bilayer structure with the Bragg reflection band centered at 15°. The different reflectivity curves correspond to the given structure with a number of layers given by: a) 1, b) 5, c) 10, d) 20, e) 50, f) 100.

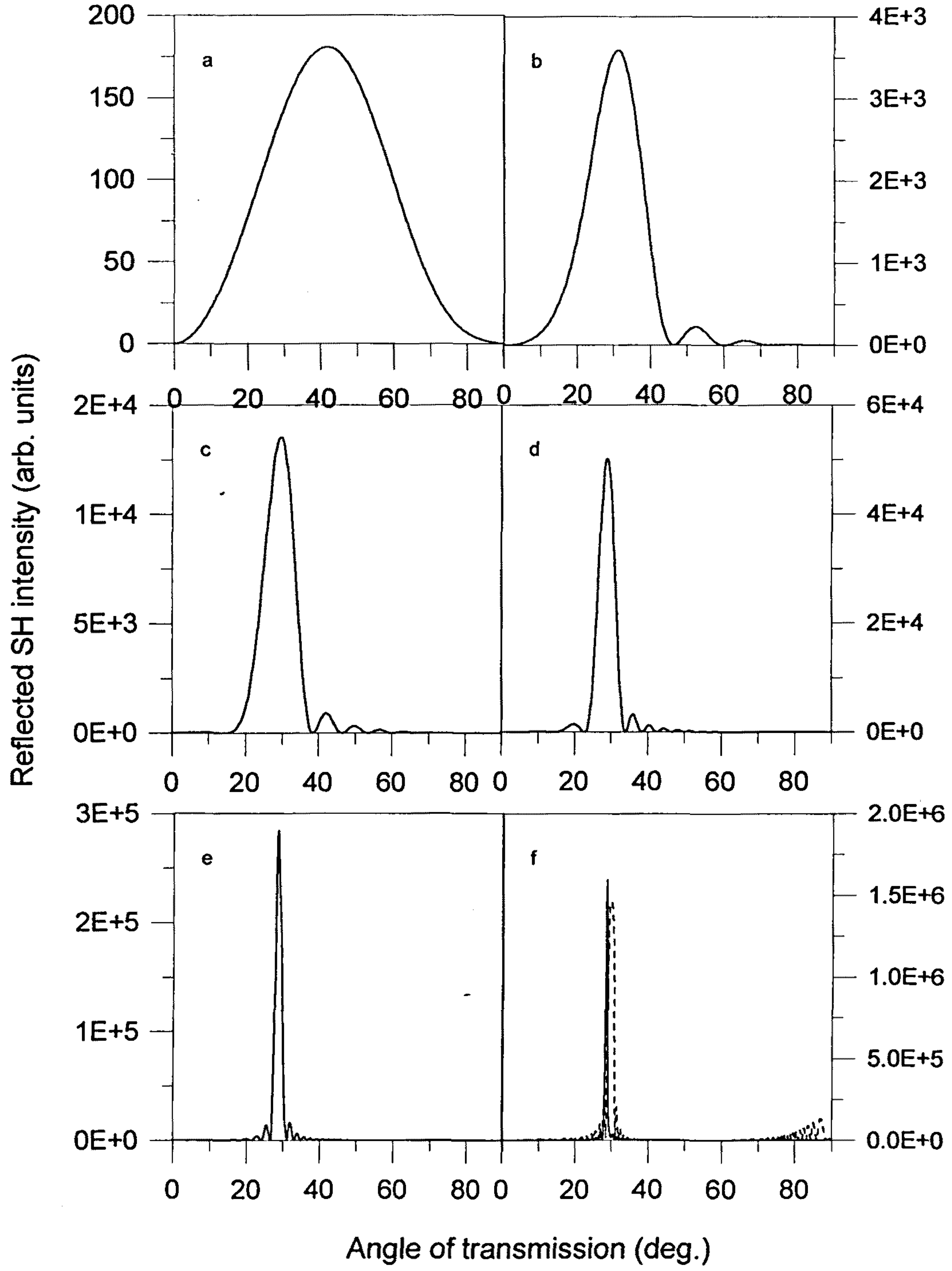

Figure 4.13 Reflected SH intensity as a function of the transmission angle for a bilayer structure with the Bragg reflection band centered at 30°. The different reflectivity curves correspond to the given structure with a number of layers given by: a) 1, b) 5, c) 10, d) 20, e) 50, f) 100.

centered at some point in the low angular band edge of the Bragg reflection band as showed in Figure 4.12 (f). The exact position of the resonance depends on the characteristics of the structure such as material dispersion. The bilayer separation in Figure 4.13 has been increased to obtain a gap centered at 30 degrees. The series in Figure 4.13 shows how in this case, the sharp resonance generated by the phase-matching process introduced by the structure appears at the band edge of the new Bragg reflection band. Comparison of both reflection curves for N=100, Figures 4.12 (f) and 4.13 (f), shows how the SH signal increases as the angle increases as demonstrated experimentally in Figure 4.6.

In order to see how this phase-matching mechanism enables the enhancement of the radiated SH intensity, we study how this reflected SH radiation changes as the number of layers is increased for different incidence angles. Figure 4.14 shows the reflected SH intensity from the same bilayer structure of Figure 4.13 as the number of bilayers is increased for three different transmission angles a) 28.97°, corresponding to the angle at which phase-matching is obtained, b) 28.5° and c) 28°. It may be seen in the figure that for the phase-matched case (Figure 4.14 (a)) a quadratic increase in the SH intensity occurs as the number of layers is increased while a change in the angle of incidence results in a very strong effect on the SH radiated by the structure. It may be seen that if we move 0.5 degrees from the resonant case the resulting SH intensity becomes considerably lower that for the phase-matched angle. By moving one degree apart from the resonant angle (Figure 4.14 (c)) it may be seen that the SH intensity is reduced to 60 times of its resonant value when we have 175 layers in the structure. This behavior is in accordance with a process of phase-matching leading to the growth of the SH intensity. This process is strongly dependent on the material dispersion of the structure which affects not only the strength of the effect but also the location of the angle at which this phase-matching takes place.

Although we have seen how this simple model recovers the main characteristics of the quadratic nonlinear process, we should include the effects of absorption and diameter dispersion of the spheres in order to have a more realistic model that accounts for the essential characteristics of the experiment. The effect of scattering losses, real absorption by the materials of the structure and the presence of defects within the ordered colloidal suspension may be included in the introduction of an effective

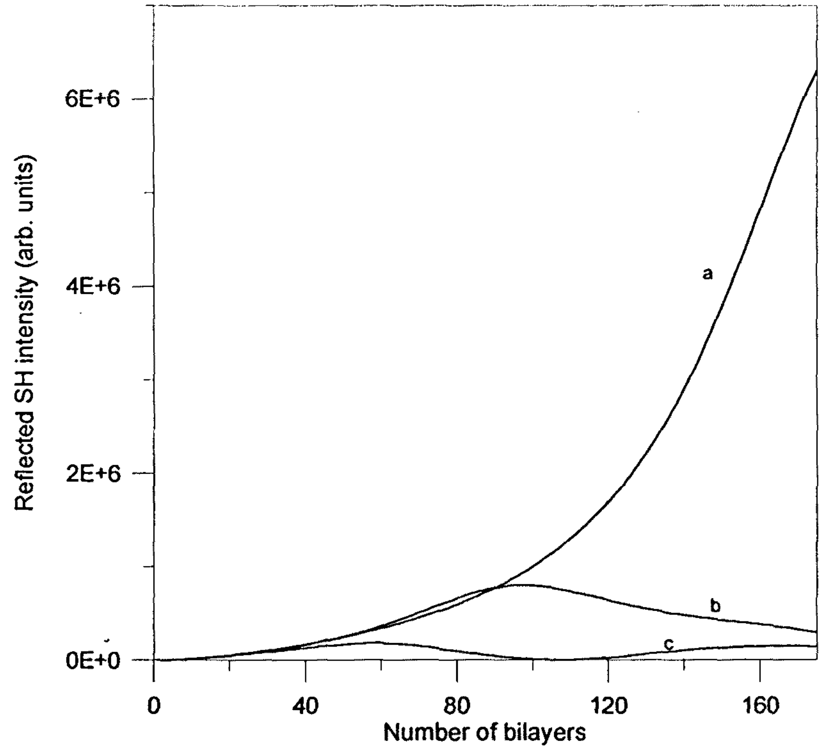

Figure 4.14 Reflected SH intensity for a structure made of bilayers identical to those of Figure 4.12 and 4.13 as the number of bilayers is increased for three different values of the angle of transmission a)28.97° (phase-matched case), b) 28.5° and c) 28°.

absorption coefficient for the structure. In order to include this in our model, we assume that the wavevectors for the fundamental and SH frequency at each layer posses an imaginary part given by

$$k_j^{2\omega} = \frac{n_j^{2\omega} 2\omega}{c} + i\frac{\alpha_{2\omega}}{2}$$

and 4.8.

$$k_j^{\omega} = \frac{n_j^{\omega}\omega}{c} + i\frac{\alpha_{\omega}}{2}$$

where $n_j^{2\omega}$ and n_j^{ω} are the index of refraction in medium j (j=0,1) at the SH and fundamental frequency respectively, and α_ω and $\alpha_{2\omega}$ are the absorption coefficients defined in Eq. 4.2 for the fundamental and SH frequencies respectively.

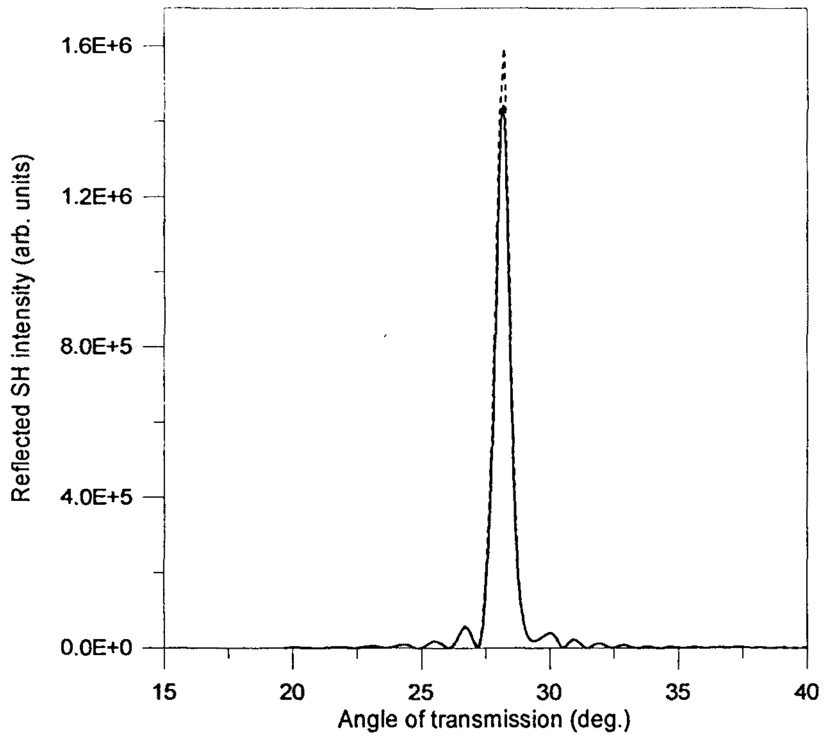

Figure 4.15 Reflected SH intensity as a function of the angle of tramsmission for the bilayer structure shown in Figure 4.13 (f) for zero absorption coefficients (dashed line) and with absorption coefficient of 40 cm^{-1} and 3.6 cm^{-1} for the SH and fundamental frequencies respectively.

Since the nonlinear monolayers are considered to be very small compared to the wavelength, we assume no absorption in the nonlinear monolayers in the model, so all the absorption effects are accounted for in the linear layers of the bilayer structure. The reflection and transmission of the structure may be derived now by including the imaginary part of the wavevectors in the model. Since the absorption is not very large we still may assume the radiation propagating in a well defined direction at each layer which is given by Snell's law.

The effect of including absorption in the model results in two clear effects in the reflected SH intensity. First, a decreasing of the SH reflected intensity is observed when compared with the zero absorption case as may be seen in Figure 4.15 in which the reflected intensity of the 100 bilayer structure in 14.13 (f) is compared to the reflectivity

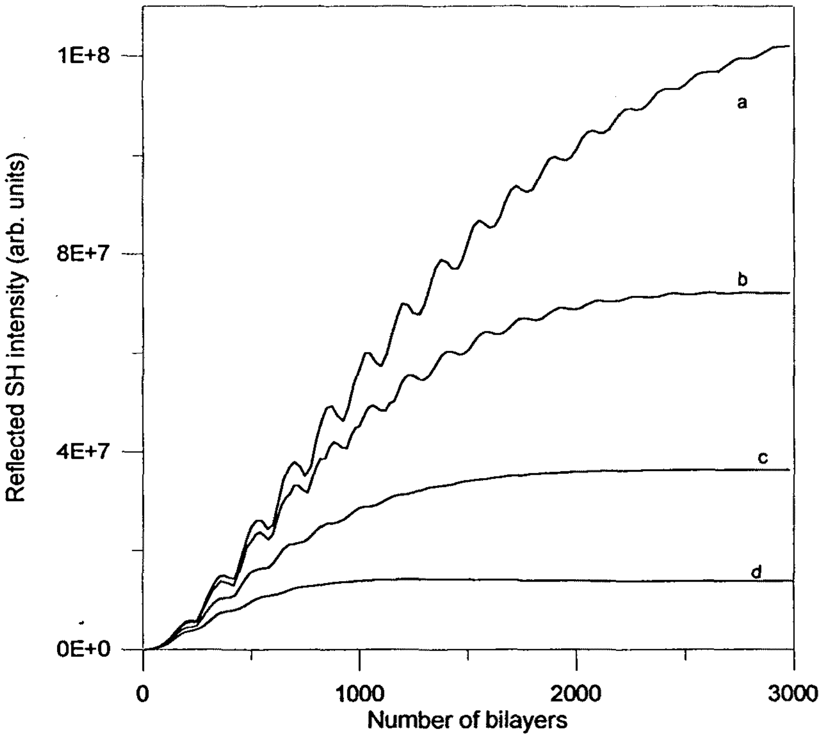

Figure 4.16 Reflected SH intensity as a function of the number of bilayers for the structure of Figure 4.14 for different values of the absorption coefficient at the SH frequency: a) 25 cm^{-1}, b) 45 cm^{-1}, c)70 cm^{-1} and d) 100 cm^{-1}. In all cases the absorption coefficient for the fundamental beam is 5 cm^{-1}.

of the same structure with an absorption coefficient of 45 cm^{-1} for the SH and 3.6 cm^{-1} for the fundamental frequency (these values are close to those measured in the colloidal crystals). It may be observed from this figure a decrease of roughly a 10% in the maximum SH reflectivity in 100 layers of the structure.

The second effect introduced by the nonzero absorption in the model is that the reflected SH intensity saturates as the number of layers is increased. This effect may be observed in Figure 4.16 where the maximum reflected SH intensity as a function of the number of layers for the same bilayer structure of Figure 4.13 is shown for different values of the absorption coefficient at the SH frequency ranging from 25 cm^{-1} to 100 cm^{-1}. It is clearly observed from these curves how the reflected SH intensity does not increase quadratically with the number of layers, but becomes saturated as the number of layers is increased. The saturation value and the number of layers at which this saturation is achieved depends on the particular value of the absorption coefficient. For the bilayer structure used in Figures 4.13 to 4.16 saturation is reached at about 2000 layers when the absorption coefficient takes a value within the range of the measured experimentally. This effect must be taken into account in crystals made of more layers, since in this case the effective length of the crystal contributing to the quadratic process should be lower than the real length of the crystal.

The curves shown in Figure 4.16 show an oscillation that becomes larger as the absorption coefficient is reduced. In order to find out the origin of these oscillations in the reflectivity curves of this bilayer model, we may calculate the reflected SH intensity by the structure when the number of layers is varied over one of these periods. This behavior may be seen in Figure 4.17 for different number of layers corresponding to a particular oscillation. It is seen from these curves that the maximum reflectivity is not always found at the same angular position, but oscillates between two values separated about 0.2 degrees. The maximum reflectivity during this angular periods shows also an oscillatory pattern which corresponds to the oscillations appearing in Figure 4.16. Since the angular position at which SH radiation is maximum is fixed by the phase-matching mechanism explained previously, we may suppose that this behavior may be associated with a change in the effective refractive index of the structure as the number of layers is increased. At the same time these oscillations are seen to vary if the bilayer thickness is changed.

The effect of the dispersion of the diameter of the crystal spheres, results in the introduction of an alteration in the perfect periodicity of the lattice. In our model we introduce this effect by letting the bilayer thickness to vary randomly between a given range. The separation between the bilayers is varied in each case in order to keep the period of the structure constant. If the bilayer thickness is varied and the bilayer separation is maintained constant, thus varying the period of the structure, the phase-matched mechanism of the process is lost and the SH resonance disappears with thickness variations as low as 5% of the sphere diameter. A measure of the disorder introduced in the structure may be obtained by calculating the degree of disorder (DOD) as defined by Zhang et al.[Zha95]

$$DOD = \sqrt{\frac{1}{N}\sum_i\left[(D_i - \overline{D})^2 + (s_i - \overline{s})^2\right]}\Big/(\overline{D} + \overline{s}) \qquad 4.9.$$

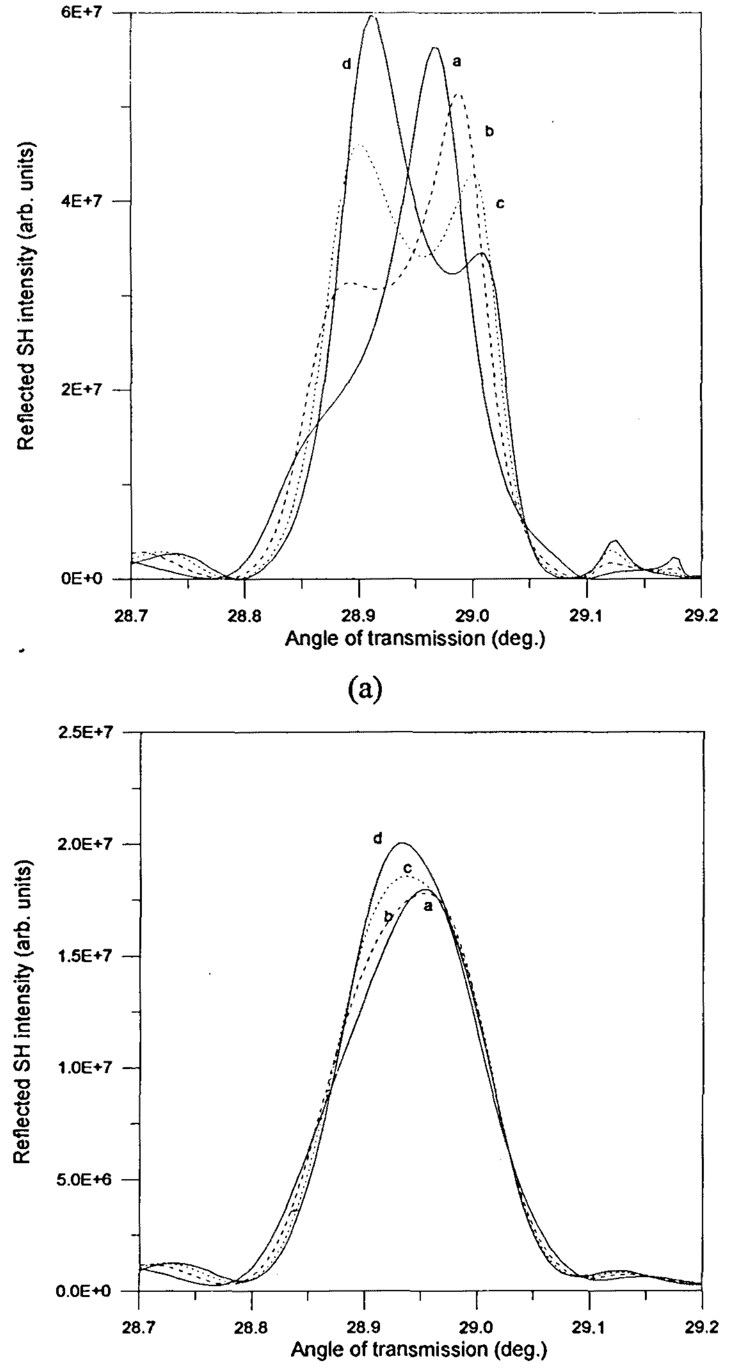

(a)

(b)

Figure 4.17 Reflected SH intensity as a function of the angle of transmission for structures made of identical bilayers with increasing number of bilayers: a) 540, b) 575, c) 600, d) 620, corresponding to one of the oscillations found in Figure 4.14. Figure 4.17 (a) the absorption coefficient is zero and Figure 4.17 (b) corresponds to the case of absorption coefficient $\alpha=45\ \mathrm{cm}^{-1}$.

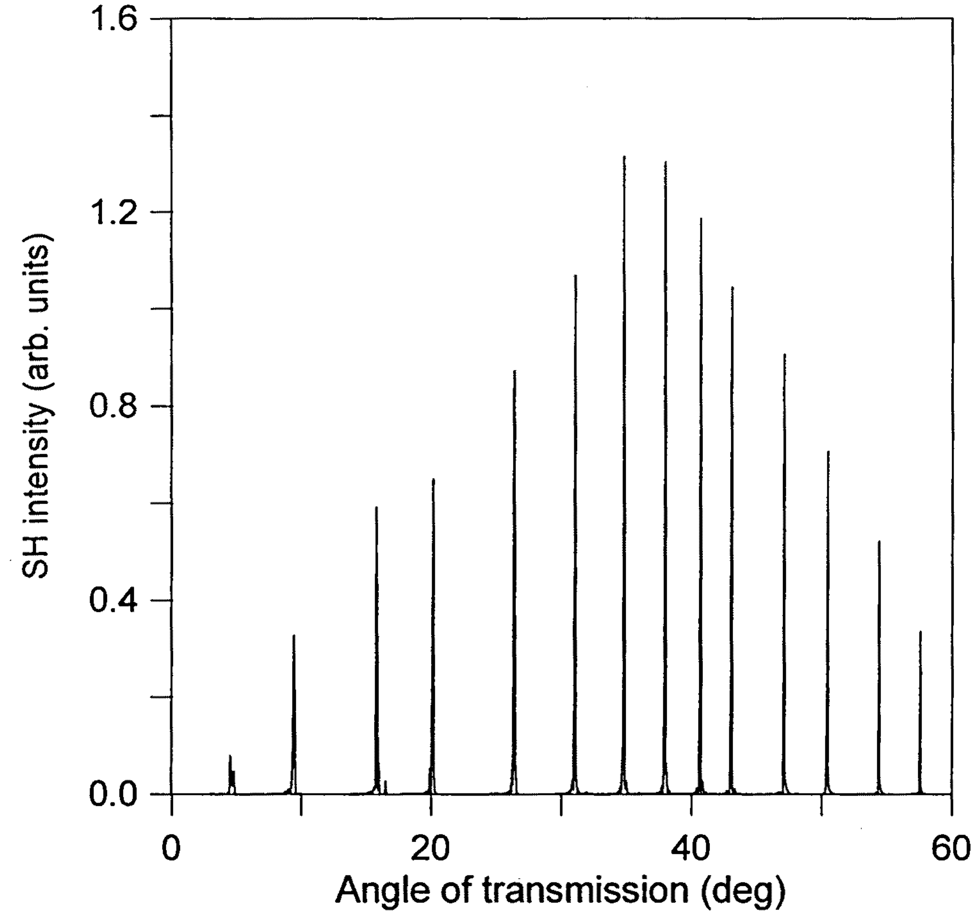

Figure 4.18 Reflected SH intensity for different structures made of identical bilayers with a increasing separation between them. Each crystal is made of 1000 layers.

Where D_i and s_i are the real thicknesses of the ith period, $\overline{D}$ and $\overline{s}$ its averaged values and N the number of bilayers. Typical values for the DOD in the model with a maximum dispersion value of 5 nm in the bilayer thickness, which represents roughly the 5% dispersion of real latex spheres, are of the order of 0.01. The introduction of a dispersion in the bilayer diameter results in the appearance of some noise around the reflectivity SH intensity curves of Figure 4.16, which reduces the oscillations appearing on those curves. This result supports the idea that these oscillations appear due to interferences arising between the multiply scattered waves at each plane of the structure introduced by the periodicity.

In order to show that the model presented recovers the main characteristics of the quadratic nonlinear process experimentally observed in colloidal crystals (surface character of the SHG process and phase-matching mechanism involved in the enhancement of such radiation) we show in Figure 4.18 the reflected SH intensity calculated from several bilayer structures made with identical bilayers but with different separation between them, *s* (thus with Bragg reflection curves at increasing angles), and with an equal number of bilayers. Each one of the structures will have the resonant condition at a different angle due to the change in the Bragg curve position for each crystal. The high number of layers used results in very sharp resonances at the phase-matched angular value for each one of the crystals. As may be seen from this figure, the resulting SH intensity shows the bell shaped curve, characteristic of the surface character of the SH process, which was observed in the case of one bilayer (Figures 4.12 (a) and 4.13 (a)). In this way we note that each one of the crystals generates radiation at a very particular angle, but with a collection of these crystals we can map the whole angular radiation pattern.

4. Discussion

Once the experimental results on the SHG in colloidal crystals have been presented in section 2 and the model of bilayers has been described, the following step should be to find out if this simplified model of the real interaction agrees with the observed results in the experimental measurements.

To simulate the experimental results with the bilayer model, first we need to find the parameters of the bilayer structure that best reproduce the real colloidal crystals. This will be done by looking at the parameter values which better fit the Bragg curves measured in section 2.2. The plane wave transfer method can also be used in the linear case to determine the effective thickness, *D*, and refractive index, n_l, that best match the experimental data points measured from the passive properties of the crystals (Fig 4.4).

In order to obtain these parameters we will make the following considerations: the index of refraction of the medium surrounding the bilayers, n_o, is taken to be that of water (1.33) and all the crystals will have the same bilayer thickness, *D'*. The different concentrations of the crystals will be given by different values of the bilayer separation, *s*. In order to find the parameters n_l, *D'* and *s* for each crystal, and to avoid a large time-consuming trial and error procedure we may set a first estimate of the unknown parameters from the experimental curves of Figure 4.4. From the coupled mode theory of multilayer structures [Yariv] an expression may be derived for the angular width of the reflectivity gap of such structures, which is directly proportional to the index contrast of the structure. Since we have fixed the value of the index n_o, we may obtain an approximate value for n_l by using the following expression derived from the coupled mode theory:

$$n_1 = n_o \sqrt{\frac{1+F(\theta)}{1-F(\theta)}} \qquad 4.10.$$

with $F(\theta) = \frac{\pi \cos\theta_B \Delta\cos\theta}{2\cos(2\theta_B)}$.

Where θ_B corresponds to the angular value at which the Laue resonance for each crystal is found and $\Delta\cos\theta = \cos\theta_1 - \cos\theta_2$. The angles θ_1 and θ_2 are the angles delimiting the gap width at $0.87R_{max}$ [Yariv]. This expression is valid for structures with equal thickness for all its layers. Nevertheless, it has been used as a first approximation to the value of n_l that may be obtained for the experimental measurements since, as we will see, the thicknesses of the layers in the resulting bilayer structures will be similar. After some trials with index values close to that found with expression 4.10 we can fit the angular width of the resulting reflection band of the bilayer structure. The angular position of the Bragg curve may be fitted by adjusting the value of the thicknesses *D'* and *s*. With this procedure, a best match is found for each one of the crystals of the experimental configuration by taking the values sumarized in the following table:

Laue angle	n_l	n_o	D(nm)	S(nm)
12	1.369	1.33	111.3	90
15.5	1.368	1.33	111.3	93
16.7	1.368	1.33	111.3	94
19.5	1.368	1.33	111.3	97
22	1.368	1.33	111.3	101
29.7	1.367	1.33	111.3	114
34.3	1.367	1.33	111.3	123
36.2	1.367	1.33	111.3	132

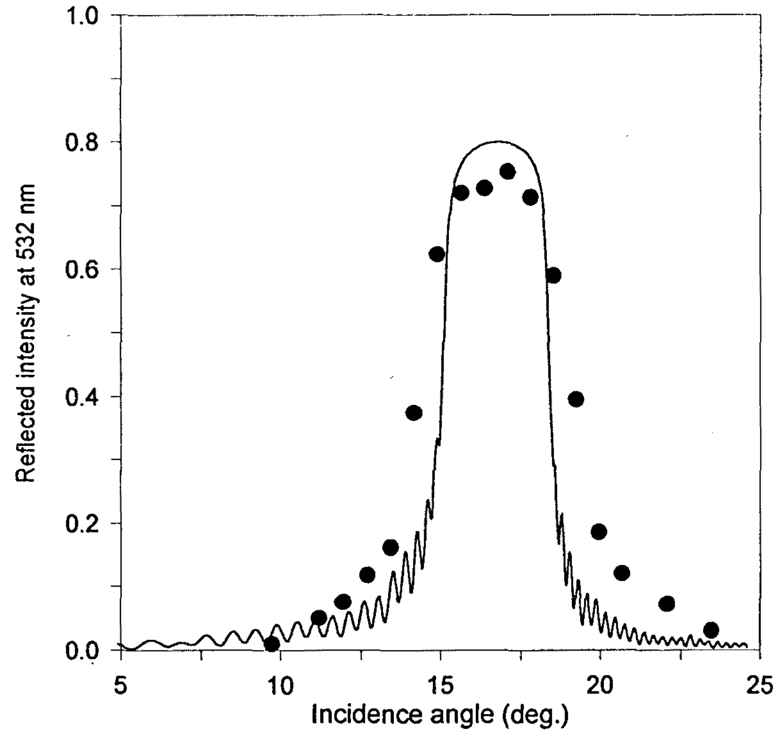

Figure 4.19 Bragg-reflection band for one of the colloidal crystals. The circular dots correspond to the experimental values measured for crystal (c) of Figure 4.4, and the solid curve is the theoretically calculated Bragg-reflection band for the crystal made of 500 bilayers with the corresponding values found for the adjustment.

Note that a best match is found with a D value slightly lower than the real value of 115 nm. Note also, that the refractive index of the nonlinear bilayer slab is considerably smaller than the refractive index of polystyrene, 1.59. This fact reflects that the coupling coefficient between planes of spheres is much smaller than the same coefficient for a similar periodic structure made of plane dielectric layers (the coupling coefficient or the directly related Bragg bandwidth in the case of an fcc lattice was derived by R.J. Spry et al. [Spr86]). Figure 4.19 shows the results corresponding to the Bragg stop band for light at 532 nm incident at one of the bilayers with the parameters found, together with the experimental data for the corresponding colloidal crystal.

The values of the effective absorption coefficient introduced to account for the losses introduced by defects in the crystal lattice, dispersion in the sphere diameter and absorption by the dye molecules are taken from the experimental measurements of section 2.4 (Figure 4.8) for each crystal. This effective absorption coefficient ranges

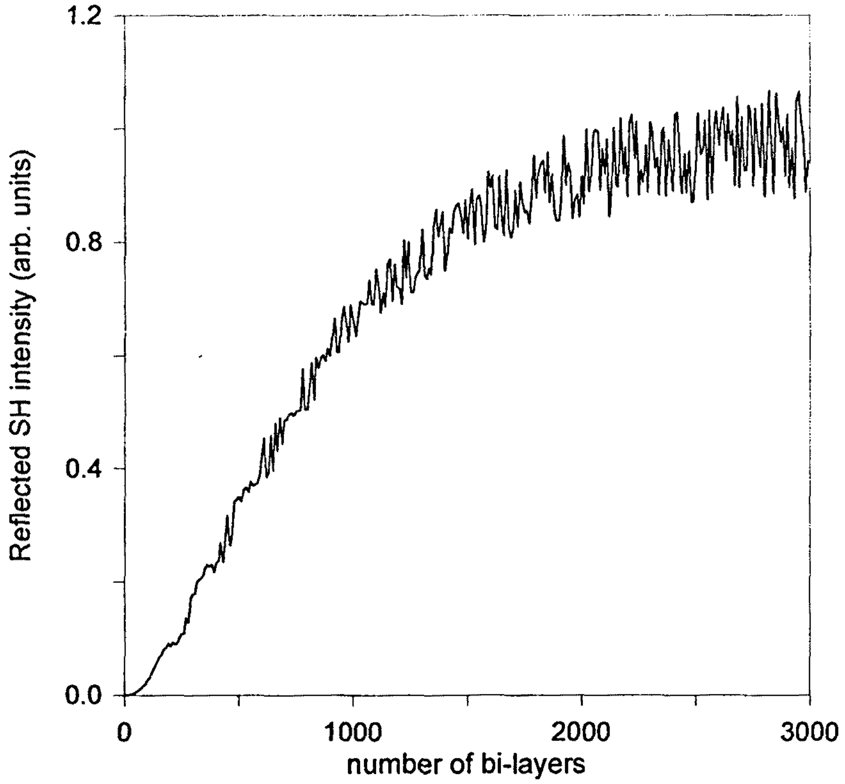

Figure 4.20 Reflected SH intensity from a crystal of plane bilayers as a function of the number of layers. This numerical result was obtained considering a 5% dispersion in the length of the nonlinear slab and an effective absorption coefficient of 46 cm^{-1} for the SH and 3.6 cm^{-1} for the fundamental in the model.

from 45 cm^{-1} from the crystal with the lowest concentration of spheres up to 60 cm^{-1} for the crystal with the largest concentration of spheres at the SH frequency and from 3.4 cm^{-1} to 5.5 cm^{-1} for the fundamental frequency. A 5% dispersion in the diameter of the spherical polystyrene particles is accounted for in our model by the introduction of a 5% random variation of the thickness of the nonlinear bilayer slab but keeping the total thickness of each period constant. Both the effective absorption coefficient and the 5% random variation limit the maximum available length for a continuous growth of the SH field.

As shown in Figure 4.20, when SHG is considered in a reflection geometry from a bilayer structure using the corresponding effective absorption and other parameters available from the measurement of the passive properties of the crystals, the intensity for the reflected SH saturates approximately after 2500 bilayer slabs. This corresponds to a crystal length of 0.5 mm, half the length of the 1-mm path length samples used. In

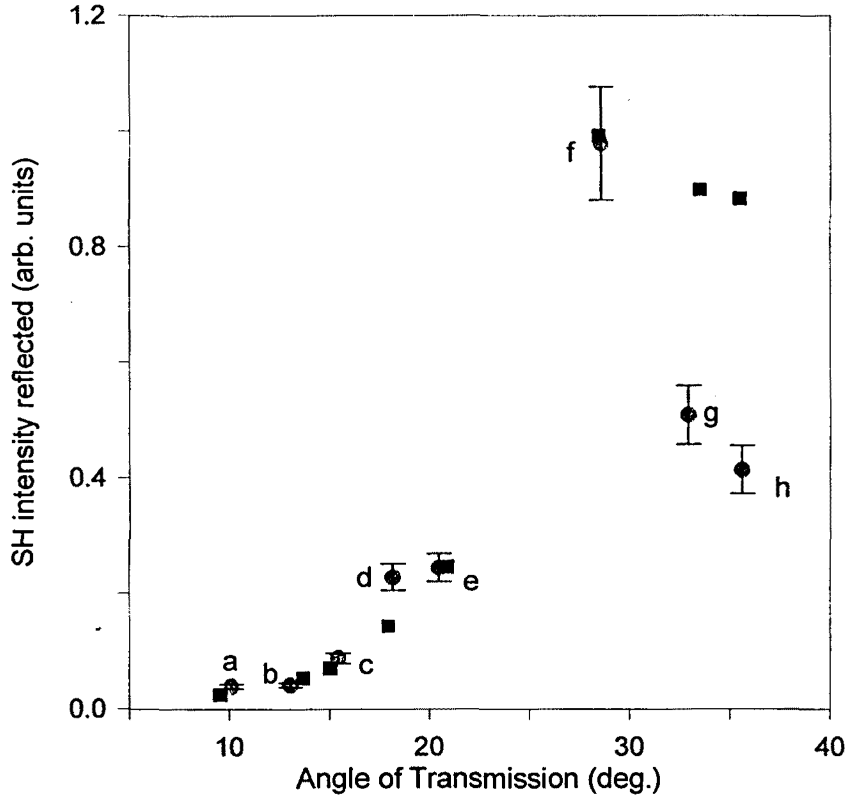

Figure 4.21 Reflected maximum SH intensity from the eight crystals of Figure 4.6. The circular dots correspond to the experimentally measured values, while the solid squares represent the values for maximum SH intensity obtained from the numerical calculation with the bilayer model described in the text.

view of this result, we should use in the numerical simulation of the experimental data structures made of 2500 bilayers. The only adjustable parameter, not derived directly from the experimental measurements, used in the numerical calculations to determine the intensity of the reflected SH field by the bilayer structures is the ratio between the nonzero elements of the nonlinear tensor corresponding to the $C_{\infty v}$ symmetry; once this ratio is determined, it is maintained for all the crystals that were experimentally tested.

Figure 4.21 shows the peak of maximum SHG for each crystal determined from the numerical calculations (performed with the model described and with the parameter values found in this section) as square solid dots together with the corresponding angles at which maximum SH generation occurs for the experimentally measured crystals shown in Figure 4.6, with the corresponding error bars. As seen in this figure, we found a very good agreement with the experimental data points for the angular position as well as the magnitude of the peak within a wide angular range. However, as the angle between the reciprocal lattice vector and the wavevector of the SH beam increases, the measured peak of the maximum SHG is smaller than the prediction from our theoretical model. This can be attributed to the plane wave character of the model, which neglects the decrease in overlap between the incident and reflected beam as the angle between the reciprocal lattice and the wavevector increases. In addition, at large angles, contribution from molecules located on the sides of the sphere increases, while at the same time, contribution from molecules on the front and back decreases. Such an effect introduces at large angles an effective change on the ratio between the several nonzero elements of the $C_{\infty v}$ symmetry nonlinear tensor.

As seen in Figure 4.21, the angle of phase-matching predicted by the theoretical analysis, based on a planar periodical distribution of dielectric material, is in close agreement with the experimentally measured angle of maximum SH intensity. In Figure 4.22 we show in greater detail the phase-matching peak corresponding to the crystal that gives the largest SHG. Notice that the angular width of the measured phase-matching peak shown in Figure 4.22 is 12 times larger than the predicted FWHM from the numerical analysis that considers 2500 nonlinear bilayer slabs as the ones shown in Figure 4.10. This can be attributed on one hand to inhomogeneities found in the crystal lattice that limit the length of perfect phase-matching, and on the other hand to the beam divergence of a focused Gaussian beam. Given the parameters of the experimental setup, we found an angular beam spread of 0.6°, which would lead to a broadening of the phase-matching peak approximately equal to the one that is found experimentally.

In conclusion, the angular dependence of the SH intensity generated in a photonic crystal reported in this chapter is explained with the use of a model that considers surface layers of nonlinear material as the sole contributor to the nonlinear process. The symmetry breaking at the surface between the two dielectric materials that compose a photonic crystal, leads to a nonvanishing quadratic nonlinear susceptibility in the dipole approximation, that is shown to be the essential contribution to a macroscopic nonlinearity distributed in the bulk of the entire crystal. It is also shown that a continuous growth of the SH field generated at such surface is possible in photonic

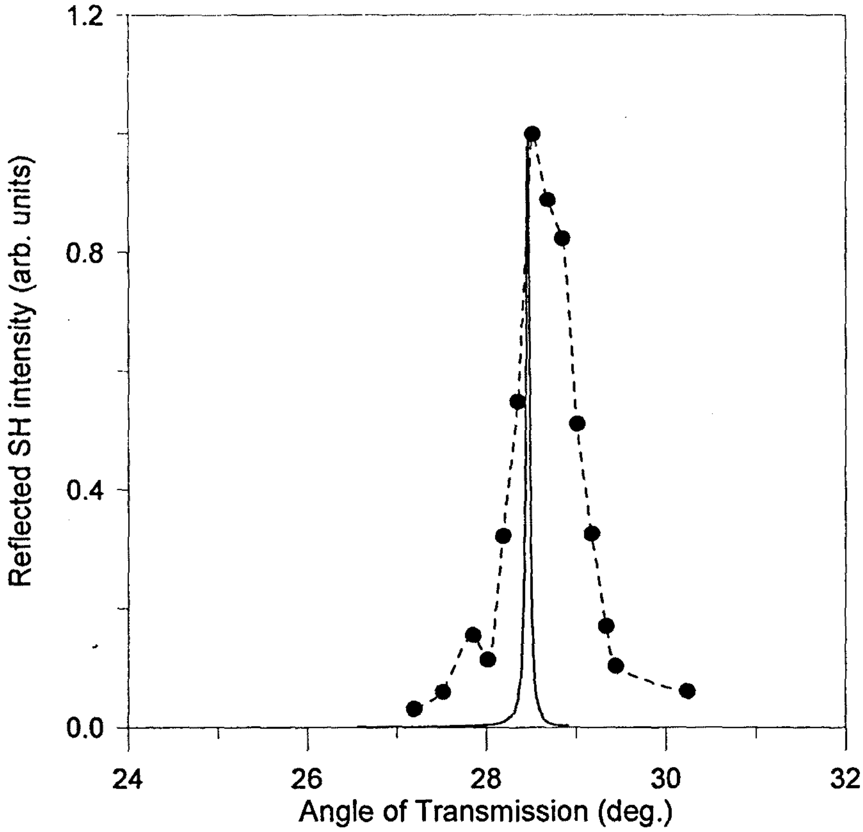

Figure 4.22 Reflected SH intensity for crystal (f) of Figure 4.6. The experimental values measured are represented in circular dots (the dashed curve is only a guide for the eye), and the solid curve is the reflected SH intensity obtained from the theoretical model for a 2500 bilayer crystal with the parameters measured from the passive properties of the crystal (f).

crystals because of the phase matching mechanism that is inherent of periodic distributions of linear dielectric material. In addition, we have determined that the effective absorption as a result of the dispersion in size of the spherical particles that compose the periodic structure, is the major limiting factor for a more rapid growth of the second harmonic generation. One of the major interests of this SHG process is its great versatility since the quadratic radiation process (by the dye coated spheres) is separated from the phase-matching process (originated from the periodicity of the structure).

Chapter 5

Conclusions

We have presented in this work an experimental and theoretical study of the second harmonic generation in photonic crystals, in order to demonstrate the effect of the environmental conditions in the resulting radiated intensity from the nonlinear dipoles. Experimental evidence of the importance of these environmental conditions on the resulting second harmonic generation from nonlinear monolayers has been obtained in two different configurations: (a) a first one in which the nonlinear material was placed within the defect of a 1-dimensional photonic crystal, and a second one (b) for which the nonlinear material was distributed over the 3-dimensional photonic crystal made of a colloidal suspension of dye coated spheres.

A) From the first configuration, the following conclusions have been obtained:

- Experimental measurements of the SH radiation from the structure when the NL slab is placed within the defect have been performed, which show sharp resonances at particular angles separated by regions where little SH radiation has been observed. By comparing these results with the intensity radiated by the NL layer when the defect is made larger than the coherence length, and most of the interference effects disappear, we observed the existence of enhancement of the SH radiation at resonances and inhibition of the SH radiation at other angles within the gap.

- The observed resonances are associated with two different physical processes. On one hand, the resonances appearing within the gap are consequence of the coupling of the SH radiated field to the defect-induced local modes of the cavity, its position depending of the size of the defect. An enhancement of six times the emission of the monolayer out of the structure was measured experimentally. On the other hand, the resonances appearing at the band edges are a result of the periodicity built into the material, and their location in the angular spectrum is independent of the size and position of the defect. The bending of the electromagnetic wave dispersion curve at the band edges indicates that the group velocity approaches zero, giving rise to an increased effective path length and a Van Hove-type singularity in the photon density of states, responsible of this local enhancement.

- The nonlinear interaction at other angles within the gap is inhibited by destructive interference between the total SH field generated within the structure and the oscillating dipoles at the SH frequency. This suppression of the oscillation, observed experimentally by us, constitutes an example of the inhibition of the radiation from a classical dipole source.

In order to better understand the observed effects, we developed a theoretical model describing this interaction. From the theoretical analysis of the problem, we concluded:

- The reflectivity of such structure for incident radiation at the SH frequency, 2ω, when no nonlinear slab is placed at the defect, shows an angular gap with high reflectivity and defect states appearing within the gap. The position and size of these defects depends on the defect length. When the slab is placed within the defect, sharp SH resonances appear in the reflected SHG spectrum at those particular angles where the defect modes were observed. This demonstrates that SH enhancement is obtained at those angles for which coupling with the local modes is provided.

In order to compare the experimental results and the theoretical curves we needed to measure the optical and geometrical parameters of the structures in the experiment, in order to perform the simulation. To obtain these parameters some previous steps have been necessary. From this measurement procedure we may conclude that:

- The parameters of the structure can be accurately determined using a method developed by us, explained in Appendix B, which is based on a double measurement of the reflectivity and transmission of the structure both in the angular and in the frequency domain. This method allows for a determination of the number of layers, thickness and refractive indices of quarter wavelength Bragg reflectors and could be extended easily to other kind of structures. The refractive indices may be calculated at the desired wavelength with a precision of the order of 0.01.

- We can determine the ratios among the different nonlinear coefficients corresponding to the NL slab from the experimental measurements when the two dielectric slabs are placed far from each other. The position of the local minima allow us for a determination of the coefficients by adjusting the theoretical curves to the experimental data. This point has been corroborated by performing extra measurements with a different periodic substrate.

- Once all the parameters obtained, we may calculate the SH intensity and that results in a very good fitting between the experimental measurements and the simulated curves. The numerical prediction of an enhancement of 90 times, given by the theoretical curves, however is considerably higher than the enhancement of 6 times observed in the experiments. This discrepancy probably arises from the spreading of the laser beam, diffusion by imperfections in the multilayer stacks, and imperfect parallelism of the two stacks.

From the study in chapter 3 of the interaction of the radiation of a sheet of oscillating dipoles within a 1D truncated periodic structure, considering in detail the amplitude, orientation and phase of the field vector at the position of the dipole sheet we may conclude that:

- The total SH emitted intensity from the nonlinear slab located within the defect of a 1D truncated periodic structure presents a strong variation as the slab is moved within the defect.

- The total SH emitted intensity from the structure as the slab is moved within the defect is not, in general, proportional to the field amplitude distribution inside the structure, since the phase difference between the dipole oscillation and the field plays a determining role in the process of energy radiation from the slab.

- From the calculations of the energy transfer from the nonlinear dipoles to the field at 2ω, which as expected equals the total emitted intensity from the structure, we have shown that the contributions of the forward and backward components of the field at the slab position are not symmetric and there exist conditions where one of the components is transferring energy to the field while the other is transferring energy back to the oscillating dipole. Nevertheless, the net transfer of energy from the dipoles to the field at frequency 2ω is always positive, as we only consider steady-state conditions.

- The phase difference between the radiating dipoles and the generated SH field acting on the dipoles plays a determining role in the final energy conversion to the SH field. When the energy transfer for the corresponding component of the field (forward or backward-propagating) is positive, the phase difference ranges from 0° to 180°. In contrast, when the energy transfer is negative, the phase difference ranges from 0° to – 180°, or from 180° to 360°.

- The dipole orientation plays also a determinant role in the radiative process, to the point that for a slab in a given position within the defect, we may found enhancement or inhibition of the radiation depending on the orientation of the dipoles at the slab.

- In contrast to what happens in free space, the maximum transfer of energy from the oscillating dipoles to the field does not occur exactly when the phase difference is π/2 as in free space, demonstrating that the influence of the environment is not limited to a change in the field intensity distribution.

- When the energy transfer process is studied at a particular angle where inhibition of the SH is observed, there exists positive energy transfer from the dipoles to one of the components of the field. Almost the same amount of energy is then lost by the counter-propagating component, giving as a result a total energy transfer which is lower than in free space, thus resulting in the inhibition observed.

- The analysis we performed should be useful to understand most of the fundamental features of the phenomenon of generation of optical radiation from a localized source embedded within a material structure, which is of interest not only from the fundamental point of view but also from the applied one, since microcavities and 1D photonic crystals are increasingly considered for a variety of uses. Examples include photo-emission (VCSELs, microchip lasers, organic or inorganic emissive films and LEDs, etc), optical switching, spatial soliton formation (in particular in optically driven cavities filled with a second-order nonlinear medium or a saturable absorber)

B) In the second experimental configuration, described in chapter 4, we grew 3D colloidal crystals which constitute a periodic arrangement of scatterers with Bragg reflection curves in the optical domain. From the study of the quadratic interaction at these crystals, when the NL material is distributed over the entire periodic structure (the microspheres are coated with NL organic molecules) we may conclude that:

- Experimental evidence of SH enhancement by phase-matching in a 3-D photonic crystal made of a colloidal suspension of latex spheres has been demonstrated for first time by us. The surface character of the quadratic emission and the phase-matching mechanism leading to the SH enhancement has also been demonstrated.

- By changing the concentration of dye coated spheres we have obtained several crystals with Bragg reflection curves at different angular positions. With these crystals the angular dependence of the quadratic SHG process has been studied.

- The passive properties of each one of the crystals has been determined by measuring its reflectivity for incident radiation at the SH frequency. The Bragg reflection curve obtained for each one of the crystals has helped us in the determination of the phase-matching mechanism involved in this process.

- The experimental results on the SH intensity reflected, shows a sharp resonance in the angular spectrum for each one of the crystals and that the SH resonance increases as the crystal concentration decreases up to a particular point and then decreases as the crystal becomes more diluted. This behavior is typical of surface nonlinear phenomena which are responsible of the SH generation in this case. At the same time it is observed that each one of the resonances appears at the low angular edge of the corresponding Bragg reflection curve for each one the crystals. This is in accordance to a phase-matching mechanism provided by the periodic distribution of the crystal. The change in the effective refractive index at the band edges due to the bending of the dispersion curve, introduces the necessary phase lag to match the refractive indices of the fundamental and second-harmonic wave at the low angular side of the Bragg reflection curve. This method of phase-matching in a periodic structure was proposed many years ago but has been implemented only very recently.

- Although for crystals with phase-matching conditions, a quadratic increase in the power conversion with the crystal length should be expected, this behaviour is not exhibited in the colloidal crystals used since there is an effective absorption appearing as a consequence of the scattering losses due to the presence of defects in the crystal lattice, the dispersion in the sphere diameter and the non-negligible absorption cross-section of the dye used. This fact leads to a saturation of the generated signal after a critical length of the crystal.

- The model developed retains the main characteristics of the nonlinear quadratic process observed experimentally, that is the surface character of the SHG process and the phase-matching mechanism leading to the growth of the SH beam.This model is based on a periodic structure made of identical bilayers. In this model each one of the planes of spheres is substituted by a dielectric slab coated at both sides by nonlinear monolayers. The different concentration of spheres in the real crystals is simulated by changing the separation between bilayers.

- The power conversion efficiency of the SHG process measured is about 10^{12}% for the crystal with higher reflectivity. The major limiting factor for the achievement of a higher conversion efficiency is the small effective length of the crystal contributing to the phase-matching due to the crystal losses. This power conversion efficiency could be enhanced by a factor of the order of 10^{11} by increasing the concentration of molecules at each sphere, reducing the losses so a significant length of crystal contributes to the phase-matching and by selecting nonlinear molecules with high values of the susceptibility coefficients.

- The plane bilayer model developed to simulate the experimental results shows a very good agreement for the angular position and maximum SH intensity between the experimental and simulated values. At larger angles this agreement is reduced due in part to the plane wave character of the model, which neglects the decrease in overlap between the incident and reflected beam as the angle between the reciprocal lattice and the wavevector increases. In all cases the parameters defining the bilayer structure were adjusted from the experimental results of the passive properties of the colloidal crystals.

- The angular width of the experimentally measured resonances is six times larger that the theoretical resonances, in agreement with a divergence of the laser beam in the experimental configuration of approximately 0.6 degrees, which may cause this observed broadening.

- The importance of this observed SHG process, is based on the fact that the generation of nonlinear radiation, provided by the absence of inversion symmetry at the surface of each sphere, is decoupled from the phase-matching process, which arises from the periodicity of the structure. This might allow an optimization of the process of SHG and at the same time can provide new methods to study molecule-surface interaction phenomena

Appendix A

Fresnel's amplitude reflection coefficients

The reflection coefficients at a given interface separating two media are usually derived by resolving the electric and magnetic fields of the incident wave into two orthogonal, linearly polarized components, one normal to the plane of incidence (E_{TE} or E_s), and other parallel (E_{TM} or E_p). These two components are then treated as independent cases.

For both cases, three waves-incident, reflected and transmitted-are involved and each of the three waves can be represented by an electric vector that can point in one of two opposite directions (the direction of the magnetic field is immediately obtained once the elctric field is fixed). Since each field can point in one of two opposite directions, there are eight possible arbitrary ways to arrange the three electric fields at the interface for both the normal and parallel cases. The relation between the three fields,obtained by applying boundary conditions at the interface, will ultimately provide the correct direction for the reflected field reletive to that of the incident field. Fortunately, not each case has been used, but those used have been enough to cause confussion.

For the case of TE waves, almost every author has chosen the three electric fields to point in the same direction, as indicated schematically in Figure 1(a). For the case of TM polarization, however, two different conventions are usually found in the literature. Fresnel convention assumes a direction of the fields in which the tangential components of the incident and reflected fields point in the same direction, as shown in Figure 1(b). In this way the reflection coefficients at normal incidence are the same for both polarizations. On the other hand, Verdet convention (shown in Figure 1(c)) changes the sign of the reflected field, so in this case the reflection componets for TE and TM waves are identical at glancing incidence.

In the present work, we have adopted Fresnel convention for the calculations of the reflection coefficients in all cases. The resulting equations are those shown in the text.

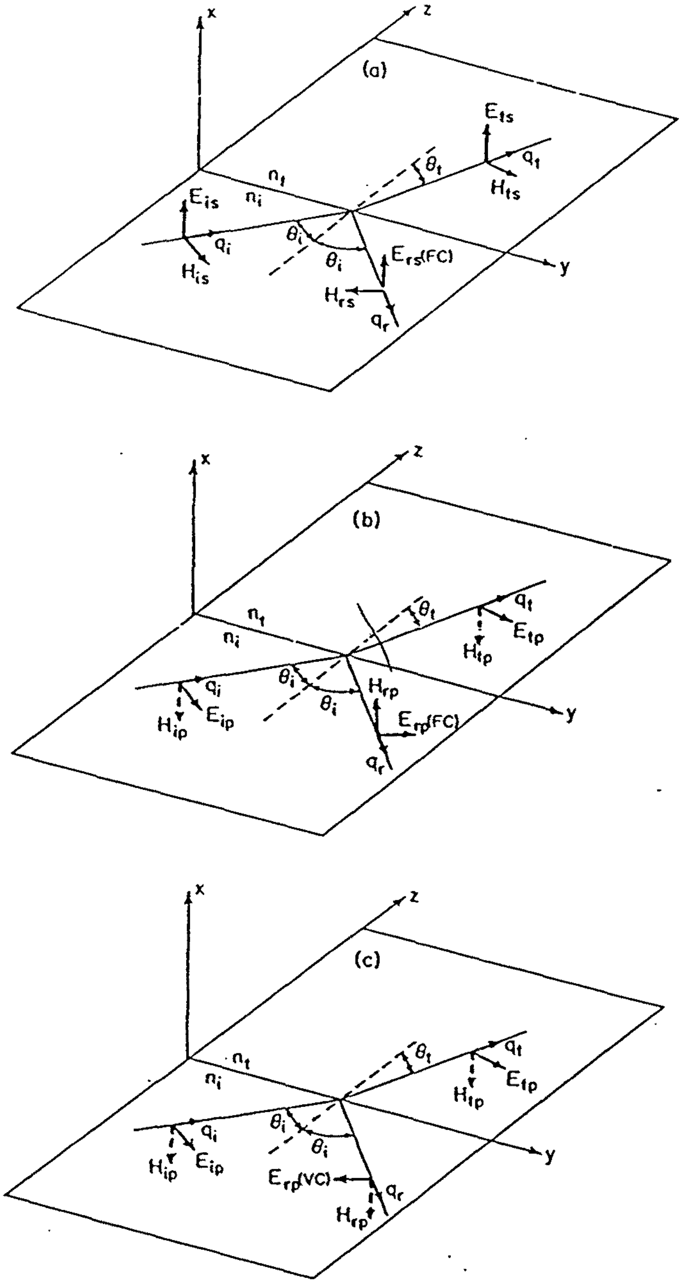

Figure 1 Conventions used to derive the Fresnel reflection coefficients. The field (*E* and *H*) and wave (*q*) vectors of the incident (i), reflected (r) and transmitted (t) waves are shown for (a) TE polarizaton, (b) TM polarization, Fresnel convention, and (c) TM polarization, Verdet convention.

Appendix B

Index determination of refractive indices of quarter wavelength Bragg reflectors by reflectance measurements in the angular domain

1 Introduction

The use of periodic dielectric structures of optical thickness smaller than the wavelength to control the properties of an electromagnetic wave has proven to be a very powerful tool with lots of potential and practical applications [Dob]. As is well known, the interference between the multiple waves arising from the reflections at the interfaces of such structures leads to the appearance of high-reflection bands for certain frequency domains of incident radiation. The position of these bands can be accurately determined from the study of the electromagnetic propagation in such structures and can be controlled by changing the structure parameters such as refractive indices, widths and number of layers used. The use of thin dielectric films in the fabrication of filters, dielectric mirrors and antireflection coatings is perhaps the most important and well known application of such structures. A particular simple structure widely used is the well known Bragg reflector, consisting of alternate layers of high and low refraction indices. In the last decade the study of more general periodic dielectric structures possessing photonic band gaps, also known as photonic crystals, has extended the application of such interference phenomena to the three-dimensional domain and their study has opened the possibility of investigating different problems related not only to classical linear optics but also to the fields of nonlinear optics (second-harmonic generation and phase matching in periodic structures, light localization) and nonlinear optical dynamics (pattern formation), quantum optics (photon-atom electrodynamics,..) and solid-state physics (band structure calculations, fabrication of structures possessing a three dimensional band gap in the optical domain).

The extensive use of these structures makes necessary their previous characterisation, i.e. the measurement of all their geometrical and optical parameters. Conventional methods to determine all these parameters exist and can be found in several review articles and references. All these methods can reproduce the different lengths and indices with high precision, but require a highly refined experimental equipment to be used. Sometimes, it is not necessary to have a detailed value of each layer and is enough to calculate the average values.

In this section we show an experimental method to measure average values of the lengths and refractive indices and to determine the number of periods of typical quarter wavelength Brag reflectors by using reflectivity measurements both in wavelength and in the angular domain. We show how these two simple measurement techniques provide complementary information to determine with good accuracy such parameters which completely characterise the structure with respect to its basic optical properties. In section 2 we review briefly the theory related with these kind of structures and outline the method used to measure their parameters. In section 3 we show experimental results obtained for commercially available dielectric mirrors at two different wavelengths and compare these results with those obtained for the same mirrors with a standard technique. Finally in section 4 the main conclusions are summarised.

2. Model

The method described in this work is used to determine the characteristics of quarter wavelength Bragg reflectors (QWBR), but it could be extended in a similar way to other kind of structures. We consider structures composed of thin lossless homogeneous dielectric slabs of equal optical thickness and with alternating high, n_h, and low, n_l, refraction indices and corresponding lengths l_h and l_l, deposited on a glass substrate of index n_s. As is usual in practice, the first and last layers will correspond to high refractive index. Such structures are known as $H[LH]^N$ structures, where N is the total number of periods in the structure, and are represented in Fig. 1.

The reflectivity and transmission of such QWBR can be calculated by the conventional method of the transfer matrix technique. The field incident on the structure will be

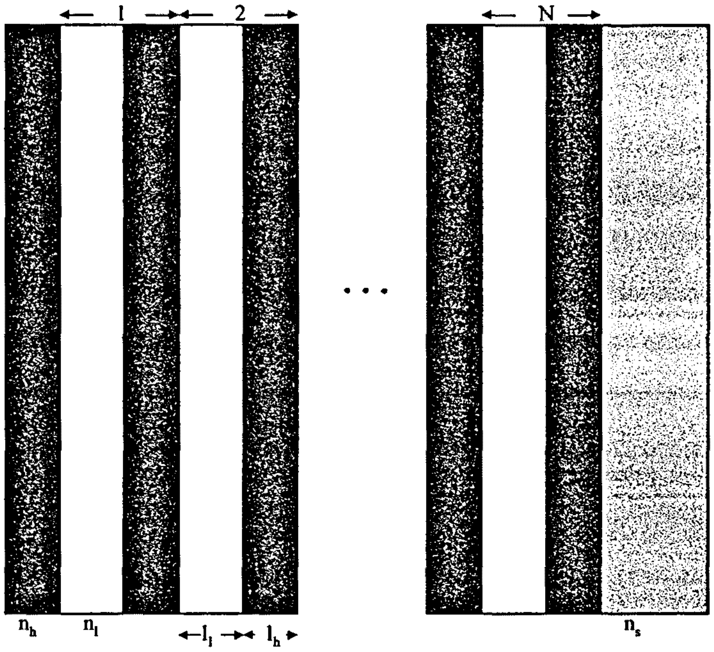

Figure 1 Schematic representation of a quarter-wavelength Bragg reflector with N periods and with refractive indices n_h and n_l and corresponding thicknesses l_l and l_h. The index of the substrate is n_s.

partially reflected and transmitted at each layer following the Fresnel laws. The resulting field in each layer can be written as a superposition of a forward propagating and a backward propagating plane waves. The field amplitudes at each layer are related through the boundary conditions at each interface by imposing the continuity of the tangential component of the electric and magnetic fields at each boundary. The propagation through one of these periods can be written in matrix form and is a representation of the translational operator of the periodic structure. Consecutive multiplication of such matrices gives a relation between the fields at both sides of the QWBR, which is used to calculate its reflectivity and transmission. For such 1-dimensional structures the two orthogonal polarizations decouple and can be calculated separately. In this paper we will suppose the incident fields with TM polarization without loss of generality, since the case of TE polarization can be treated in the same way.

Figure 2 shows a typical reflectance curve for such a quarter wavelength structure as a function of the wavelength of the incident field at normal incidence. The high-

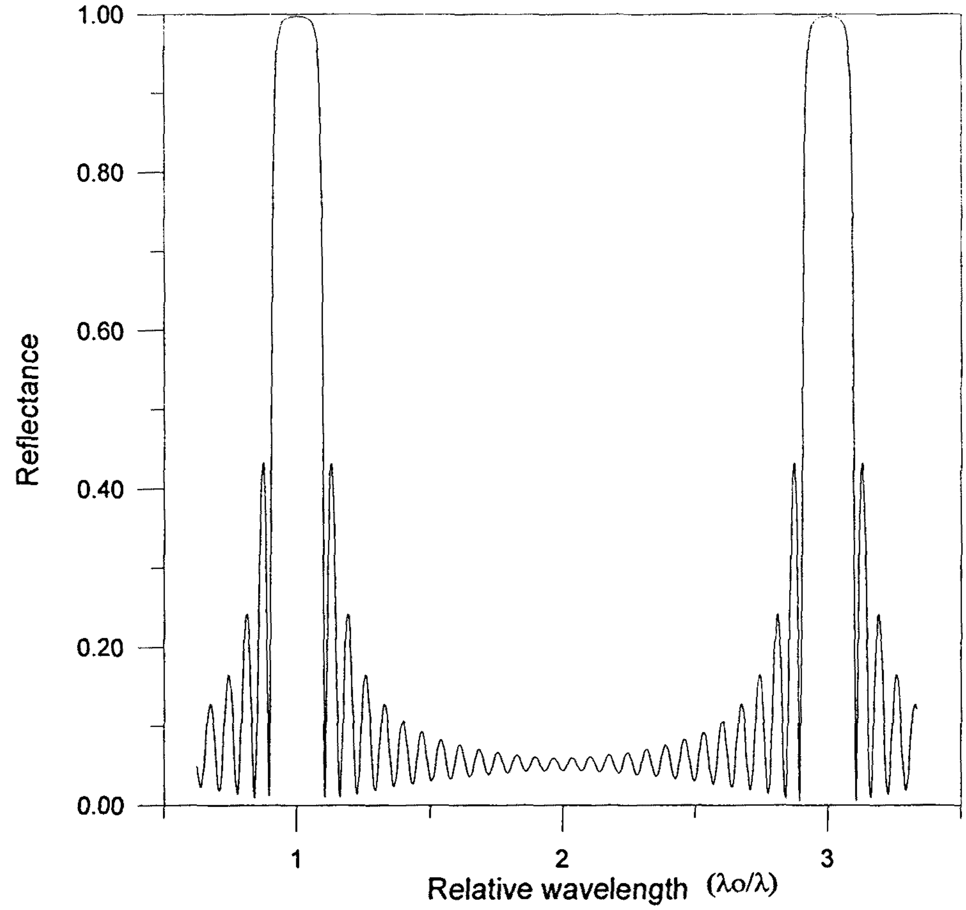

Figure 2 Reflectance as a function of the relative wavelength (λ_o/λ) for a structure made of 27 layers (N=13), with refractive indices n_l=1.4, n_h=1.8 and substrate n_s=1.53.

reflectivity zones correspond to the Bragg reflections bands. The Bragg reflection band corresponding to the largest possible wavelengths is centered at wavelength λo given by:

$$n_h l_h + n_l l_l = \frac{\lambda_o}{2} \qquad 1.$$

Other high-reflection zones appear at wavelengths satisfying the condition:

$$n_h l_h + n_l l_l = q\frac{\lambda_q}{2} \quad \text{with } q=2,3,\ldots, \qquad 2.$$

except for the cases in which the optical length of each layer satisfies the additional condition:

$$n_h l_h, n_l l_l \neq p\frac{\lambda_q}{2} \qquad \text{with p=1,2,3,...} \qquad 3.$$

In such cases there is no Bragg reflection bands. For the QWBR the optical thickness of each layer is the same, so that

$$n_h l_h = n_l l_l = \frac{\lambda_o}{4} \qquad 4.$$

This relation gives the value of the mid-gap wavelength for a given structure and according to expressions (2) and (3) other gaps will appear centered at frequencies:

$$\lambda_q = \frac{\lambda_o}{(2p+1)} \qquad \text{with p=1,2,...} \qquad 5.$$

Much smaller subsidiary resonances between such high-reflection bands appear in the reflectivity curves for the QWBR structures (Fig. 2). The number of minima in the reflectance spectrum between high-reflection bands equals the number of layers of the structure. The width of the high reflection bands is related with the index ratio n_h/n_l and increases as this ratio increases. For a given index ratio, the relative gap width $\Delta\lambda/\lambda_o$ is constant independently from the value λ_o. All these features are illustrated in Figures 3 and 4. Figure 3 shows that varying the number of periods of the structure results in the variation of the separation between subsidiary maxima. The position and width of the main gap is not changed since it depends on the optical thickness of each layer and index ratio, which remains the same for all the cases considered. Figure 4(a) shows that the gap width $\Delta\lambda$ increases when the index ratio is increased. The gap width $\Delta\lambda$ is defined as the distance between points with reflectance ρ=0.9. Fig 4(b) shows the continuous dependence of the relative gap width with the index ratio.

2.a Reflectance spectrum

This short review of the optical properties of QWBR structures shows that most of the parameters of a given structure can be obtained from an experimental measurement of its reflectance as a function of the incident wavelength at normal incidence and

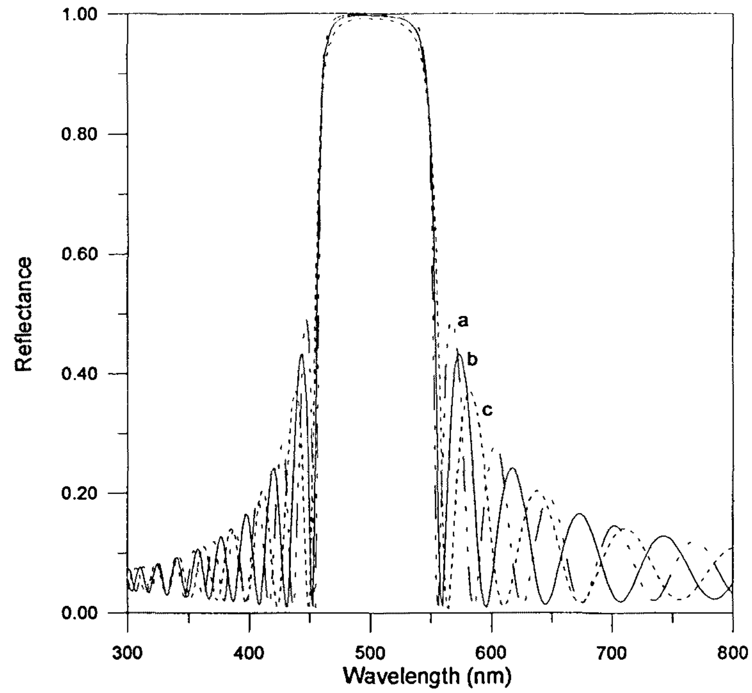

Figure 3 Reflectance curves for a structure with the values n_l=1.4, n_h=1.8, l_l=89.3 nm and n_h=69.4 nm and with (a) 31, (b) 27 and (c) 23 layers.

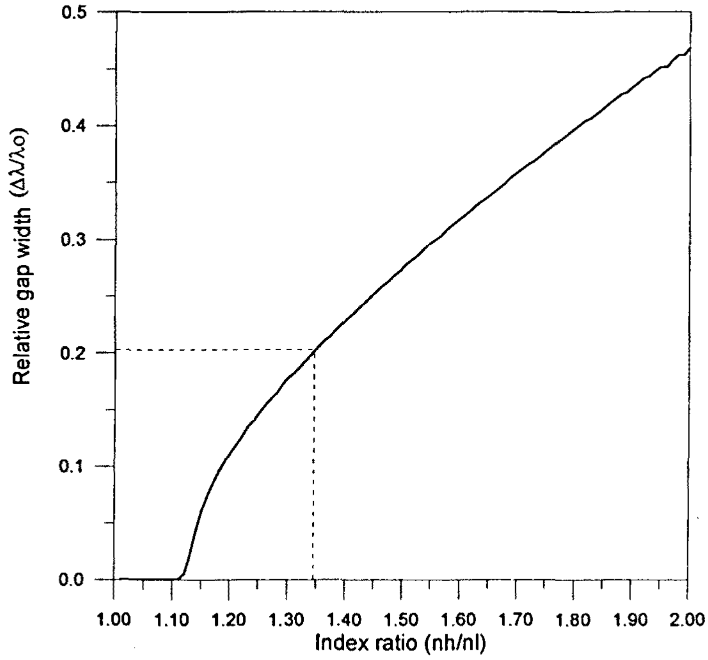

Figure 4(a) Relative gap width (measured at 90% reflectance) as a function of the refractive index ratio (n_h/n_l). The point indicated corresponds to the value found for the structure measured experimentally (section 3).

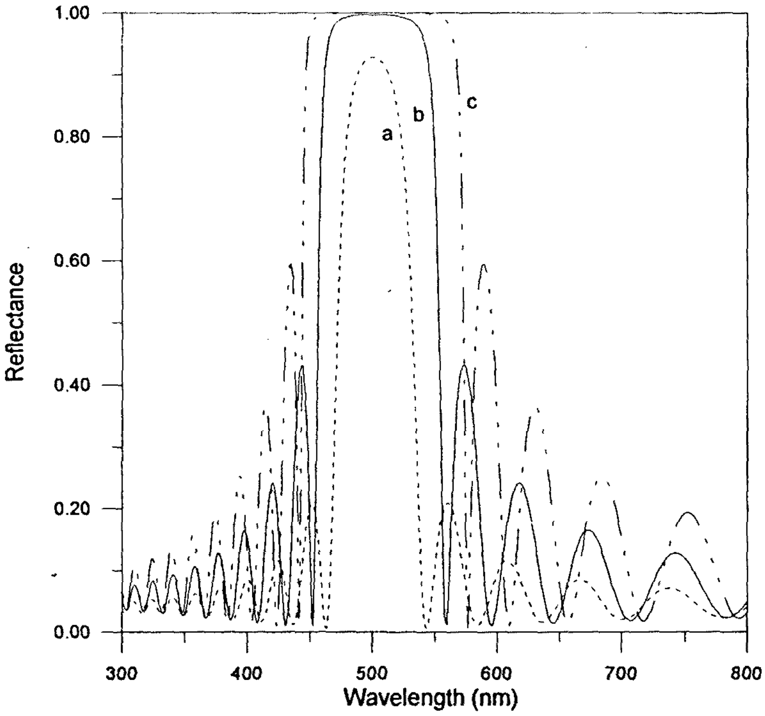

Figure 4(b) Reflectance curves for QWBR structures with equal number of layers and different index ratios (a)1.14, (b) 1.28 and (c) 1.43. The index n_l is taken to be 1.4 for the three structures and the length l_l=89.28 nm. The corresponding lengths for l_h are (a) 78.29 nm, (b) 69.44 nm and (c) 62.5 nm.

subsequent fitting to the theoretical curves here described calculated with the transfer matrix method. Specifically, the following information can be obtained:

(i) The position of the measured center-gap wavelength, λ_o, gives us the value of the optical thickness (in average) of each layer of the structure through Eq. (4).

(ii) The gap width gives the index ratio n_h/n_l according to Figure 4(a).

(iii) The number of subsidiary minima between two high-reflection bands equals the number of layers of the structure.

(iv) The values of n_h and n_l can in principle be obtained calculating the reflectance spectra for many different values of n_h and n_l (keeping the same ratio n_h/n_l) and finding the values which give the best fit to the experimental curves. At this point, however, two important remarks must be made. First, structures with different indices and with the same index ratio give very similar reflectivity curves, as can be seen in Figure 5 when the indices are close (as the refraction indices increase, the amplitude of the

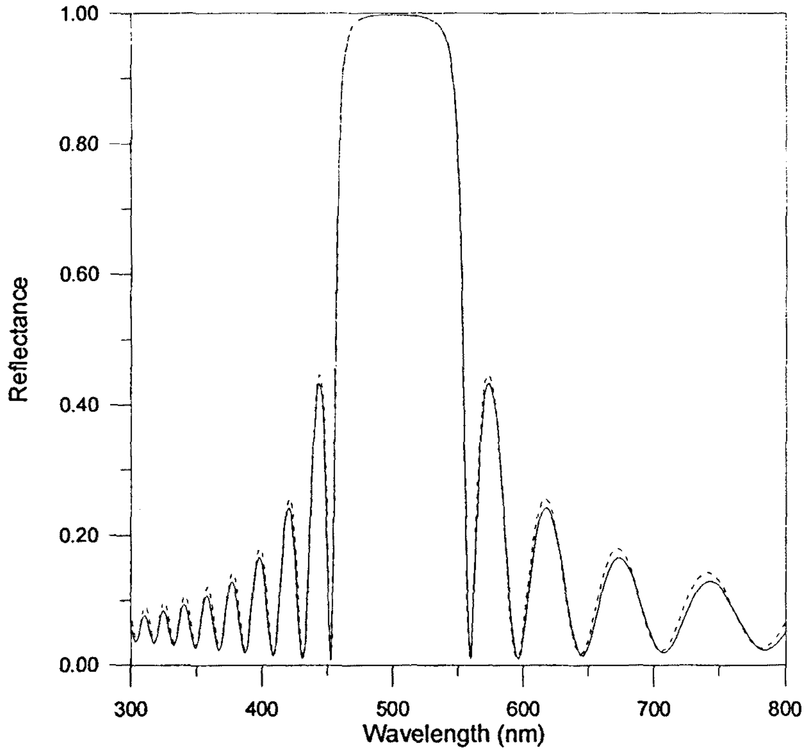

Figure 5 Reflectance curves for two structures with the same index ratio and different refractive indices. The solid line corresponds to the same structure of case (a) in Figure 3 and the dashed line corresponds to a structure with n_l=1.45 and n_h=1.86.

subsidiary maxima becomes higher). The slight difference between such reflectance curves cannot be used to discriminate the actual index value, since any real QWBR presents some imperfections which bring about noticeable distortions of the subsidiary maxima reflectance profiles. And second, if the materials used are not known, the dispersion of the material cannot be taken into account in the calculations. Dispersion makes the theoretical and experimental curves separate as the wavelength is separating from the center gap wavelength. As a consequence of this fact, it is immediately seen that the first oscillations are the ones to be considered in order to deduce the number of periods in the structure since as we separate from the high-reflection band the real oscillations will depart from that of the simulated curve without dispersion.

2.b Angular dependence

We show here that a complementary way to step (iv) above to get reliable and accurate values for the refraction indices of the materials composing the Bragg structure, for a

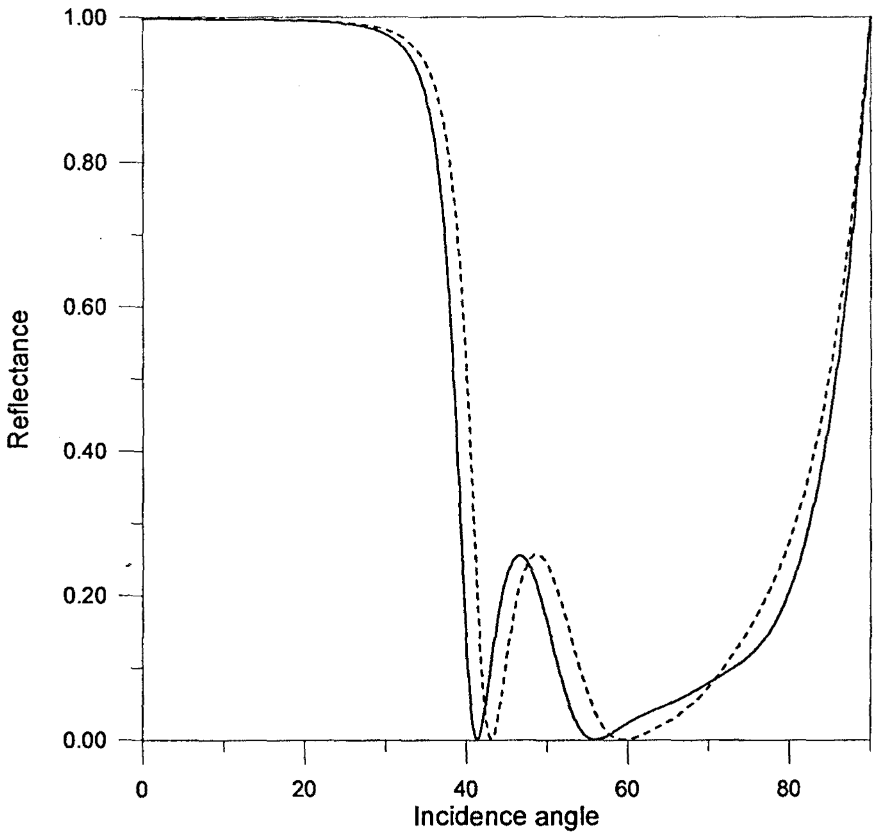

Figure 6 Reflectance curves as a function of the angle of incidence for the same structures of Figure 5 when the incident wavelength is λ=532 nm.

given wavelength, is to experimentally measure the reflectance of the structure at that wavelength as a function of the angle of incidence. This method has two advantages. First, dispersion is not present since the wavelength is fixed. And second, the reflectance curves obtained are more sensitive to the values of the refractive indices. As an example, Fig. 6 shows the reflectance curves as a function of the incidence angle for the same structure and refractive indices as those considered in Fig. 5. At normal incidence the reflectance falls within a Bragg reflection band. It can be seen that the band edges in the angular domain are very sensitive to the values of the refraction indices of the structure. In addition, we have found that some relevant details of the reflectance curves, such as local maxima or minima in the curves, at the band edges or outside the band gap, are quite insensitive to small imperfections of real structures.

3. Experimental results

We will now use the results obtained in sections 2(a) and 2(b) to determine the optical and geometric parameters of different structures. The particular QWBR used are commercially available dielectric mirrors, one of them reflecting light at 532 nm at 45 degrees and the other reflecting light at 1064 nm at normal incidence. As stated above we need two different measurements of the reflectance, one as a function of the wavelength and another as a function of the angle of incidence.

The measurements as a function of the wavelength were performed using a conventional Hamamatsu spectrophotometer that gave the transmission curves at normal incidence, in the range of wavelengths between 400 nm and 1000 nm. Figure 7 shows the experimental values obtained for the QWBR reflecting light at 532 nm. Using the approach outlined in section 2a, from these measurements we get:

(i) Since the midgap wavelength is λ_o=590 nm, Eq. (4) tells us that the optical thickness of each layer is $n_h l_h = n_l l_l = 590/4 = 147.5$ nm.

(ii) The gap width at 10 % transmission (90% reflectivity) is 120 nm, which gives a value for the relative gap width of 120/590=0.203. From Figure 4(a) this value corresponds to an index ratio of 1.346.

(iii), (iv) Now after a few trials with the theoretical curves around these obtained values one finds the values that best fit the experimental curves by fixing a value of the index n_l. Since in the experimental measurements we don't reach the wavelengths where the second gap appears, the number of layers can be adjusted by making some trials varying the number of layers. The values determined at this point from the reflectance spectrum are N=13 (N is the number of periods), $n_h/n_l=1.345$ and λ_o=590 nm.

According to section 2b, determination of the absolute values of n_l and n_h can be completed with additional measurements of the reflectance as a function of the incidence angle. The incident beam at the desired wavelength, after being passed through a polarizer in order to get the desired polarization, is incident upon the structure. The reflected and transmitted light were measured at all incidence angles and

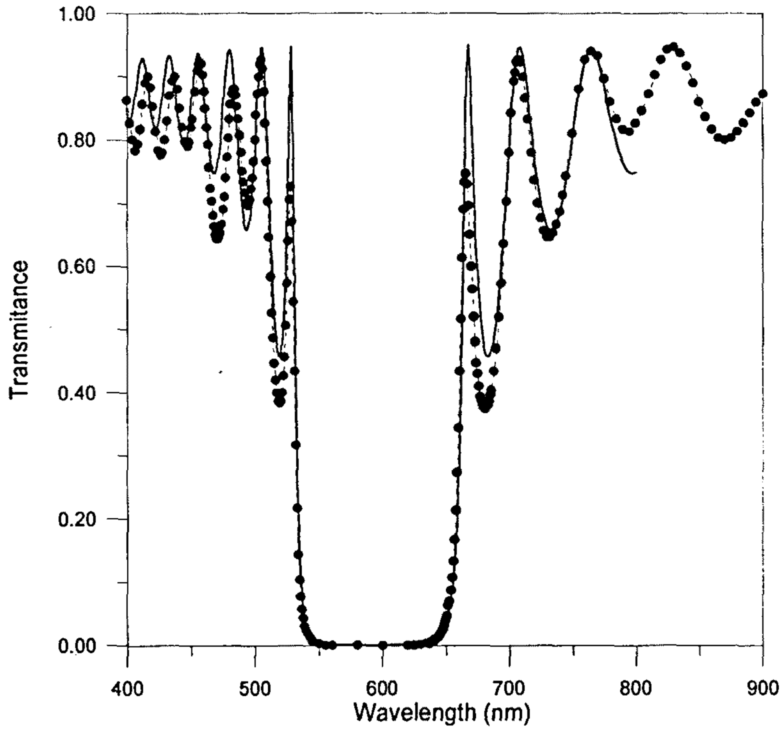

Figure 7 Measured transmittance as a function of the incident wavelength at normal incidence (dotted line) for the first mirror considered in section 3. The solid line is the curve obtained with the parameters found for the structure as explained in section 3.

both signals were added in order to have a normalisation value for the total light measured at each angle of measurement. These measurements were performed at two different wavelengths. Figure 8(a) shows the reflectance curve obtained for incident light at 514.5 nm from a cw Argon laser, together with some numerical curves obtained by setting the values obtained previously for the layer optical thickness, refraction indices ratio and number of periods, and changing the absolute values of the refraction indices. As can be seen from these curves the value of the low refraction index for this particular structure that best fits the experimental curves is found to be n_l=1.47.

Summarising, the parameters obtained for the structure are the following: the number of layers (2N +1) is 27, the refractive indices are n_l=1.47 and n_h=1.97, and the corresponding thicknesses (given through Eq. 4) are l_l=100.4 nm and l_h=74.6 nm. The numerical curve obtained with these parameters is that shown in Figure 7 (continuous line) together with the experimental results. Figure 8(b) shows the results of the reflectance of the same structure at the incident wavelength of 532 nm, showing in the same way, that the value for the low refraction index that best fits the experimental curves is again 1.47 (thus there is not noticeable dispersion between 532 and 514.5 nm).

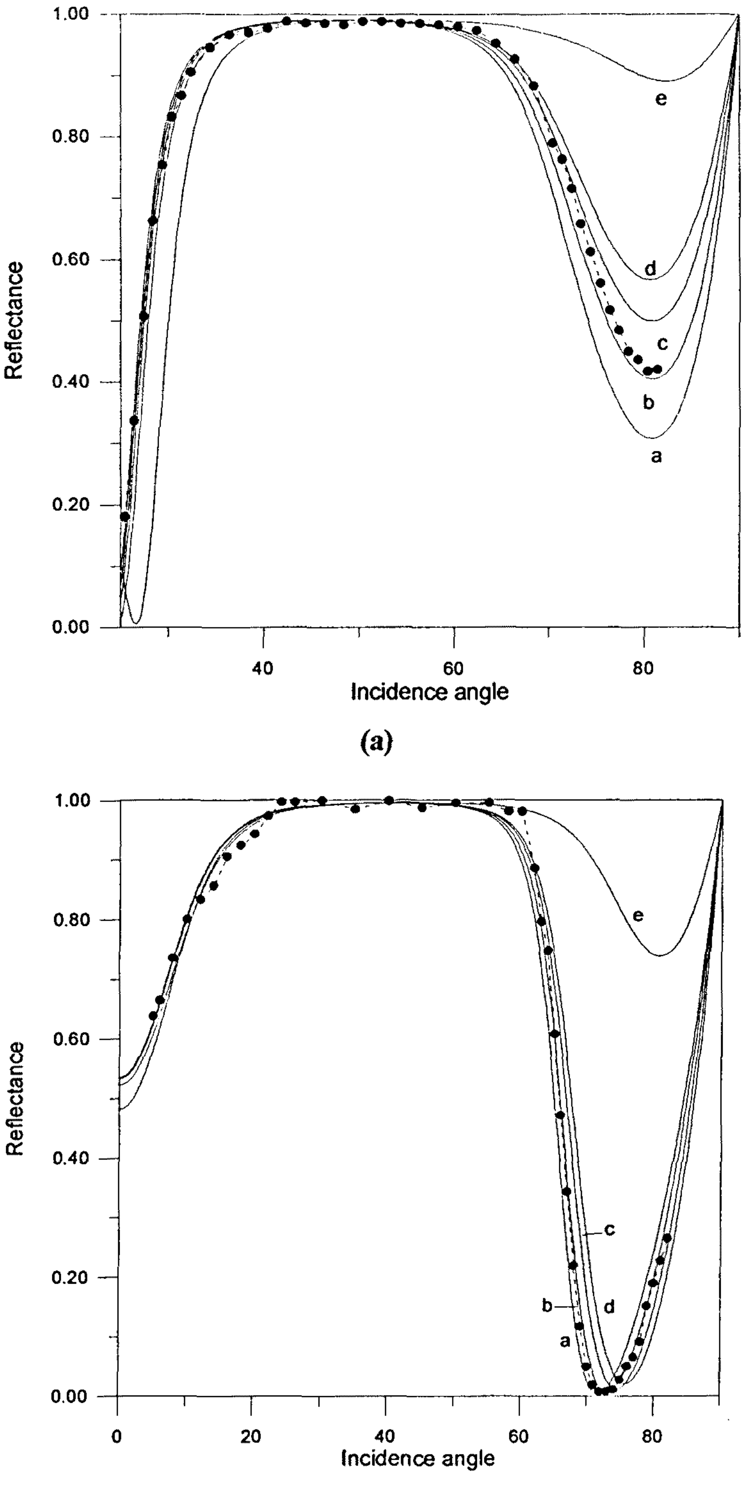

(a)

(b)

Figure 8 (a) Measured reflectance for the mirror considered in Figure 7 as a function of the angle of incidence at a wavelength of 532 nm (dotted line). The solid lines are obtained by setting the index ratio to 1.345 and the number of periods N=13 and changing the values of the refraction indices. The values for n_l are: (a) 1.46, (b) 1.47, (c) 1.48, (d) 1.49 and (e) 1.6. The values of the corresponding thicknesses are obtained in each case through Eq. (4).

(b) The same as in Fig (a), for λ=532 nm.

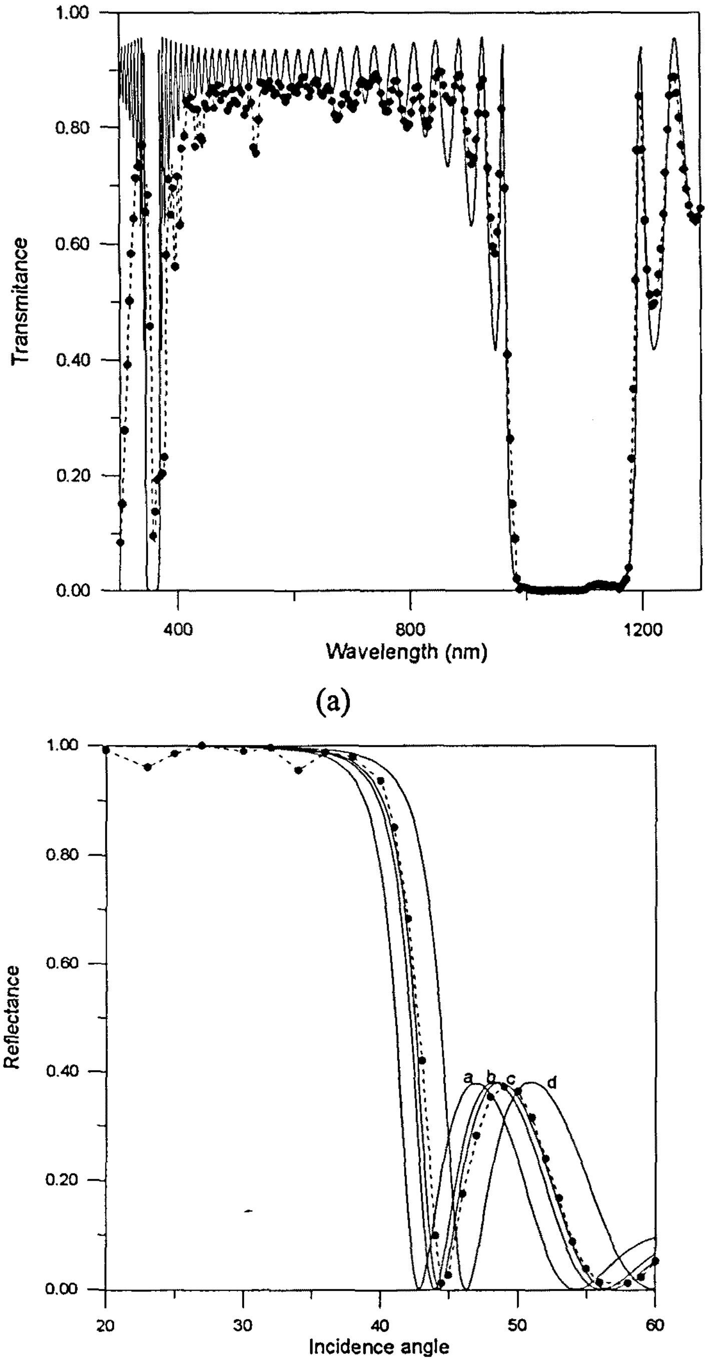

(a)

(b)

Figure 9 (a) Measured transmittance as a function of the incident wavelength at normal incidence (dotted line) for the second mirror considered in section 3. The solid line is the curve obtained with the parameters found for the structure as explained in section 3.

(b) Measured reflectance for the mirror considered in Figure 10 as a function of the angle of incidence at λ=1064 nm (dotted line). The solid lines are obtained by setting the index ratio to 1.331 and the number of periods N=15 and changing the values of the refraction indices. The values for n_l are: (a) 1.41, (b) 1.44, (c) 1.45, and (d) 1.5. The values of the corresponding thicknesses are obtained in each case through Eq. (4).

Note that these angular measurements allow us the determination of the index of refraction with a precision of the order of 0.01. This was not possible in the reflectance curves as a function of the wavelength since the distortions in the subsidiary maxima in any real mirror are higher than the separation between two theoretical curves with similar refractive indices (see Fig. 5 where the index difference between the two plots is 0.05).

In order to check the validity of the method, a characterisation of the same structure was performed through the guided optics method. Detailed information about this method may be obtained elsewhere [Mas96]. Using this method, the determination of the structure parameters gave the following results: the nstructure consists of 27 layers, with indices of refraction n_h=1.97, n_l=1.47, and averaged layer lengths l_h=75.3 nm and l_l=100.9 nm. As may be observed, the given results fit very closely the results obtained with our method.

Figures 9(a) and 9(b) show the experimental values obtained for the second dielectric mirror, which reflects light at a much longer wavelength, λ=1064 nm. In this case, since two reflection bands appear in the transmittance curve, the determination of the number of layers is facilitated. Notice also the absence of the gap at 532 nm, indicating the fact that what we have a QWBR structure. In the same way as explained previously, we obtain the corresponding parameters of this structure to be: N=15 (31 layers), n_l=1.45, n_h=1.93 and corresponding thicknesses l_l=183.8 nm and l_h=137.8 nm. The corresponding theoretical curves that best fit the experimental values are represented in Figs. 9(a) and 9(b).

4. Conclusions

We have demonstrated that determination of the refractive indices and thicknesses of quarter-wavelength Bragg reflectors is possible with a measurement of the reflectance (transmittance) of the structure both as a function of the incident wavelength at normal incidence, and as a function of the incident angle for a fixed wavelength. The measurements in the angular domain allow to determine the absolute values of the parameters of the structures with larger accuracy. To confirm the validity of the method, the values obtained have been compared to those provided by the guided optics method showing a very good agreement between them. The method demonstrated here is very easy to apply in any laboratory and thus might be of great help in fast characterisation of quarter-wavelength multilayer structures whenever necessary.

Appendix C

Expressions of the propagation matrices

In this appendix we will give the expressions corresponding to the matrices relating the fields in different layers of the truncated 1D photonic crystal, as indicated in chapter 2. (sections 2 and 3). The following expressions correspond to the TM polarization

$$[AM]=\begin{pmatrix} \frac{1}{2}\left[\frac{k_{oz}n_h}{k_{hz}n_o}+\frac{n_o}{n_h}\right] & \frac{1}{2}\left[\frac{k_{oz}n_h}{k_{hz}n_o}-\frac{n_o}{n_h}\right] \\ \frac{1}{2}\left[\frac{k_{oz}n_h}{k_{hz}n_o}-\frac{n_o}{n_h}\right] & \frac{1}{2}\left[\frac{k_{oz}n_h}{k_{hz}n_o}+\frac{n_o}{n_h}\right] \end{pmatrix}$$

$$[MA]=\begin{pmatrix} \frac{1}{2}\left[\frac{k_{hz}n_t}{k_{tz}n_h}+\frac{n_h}{n_t}\right]\exp(i(k_{hz}-k_{tz})l_h) & \frac{1}{2}\left[\frac{k_{hz}n_t}{k_{tz}n_h}-\frac{n_h}{n_t}\right]\exp(-i(k_{hz}+k_{tz})l_h) \\ \frac{1}{2}\left[\frac{k_{hz}n_t}{k_{tz}n_h}-\frac{n_h}{n_t}\right]\exp(i(k_{hz}+k_{tz})l_h) & \frac{1}{2}\left[\frac{k_{hz}n_t}{k_{tz}n_h}+\frac{n_h}{n_t}\right]\exp(-i(k_{hz}-k_{tz})l_h) \end{pmatrix}$$

$$[U]=\begin{pmatrix} \frac{1}{2}\left[\frac{k_{hz}n_d}{k_{dz}n_h}+\frac{n_h}{n_d}\right]\exp(i(k_{hz}-k_{dz})l_h) & \frac{1}{2}\left[\frac{k_{hz}n_d}{k_{dz}n_h}-\frac{n_h}{n_d}\right]\exp(-i(k_{hz}+k_{dz})l_h) \\ \frac{1}{2}\left[\frac{k_{hz}n_d}{k_{dz}n_h}-\frac{n_h}{n_d}\right]\exp(i(k_{hz}+k_{dz})l_h) & \frac{1}{2}\left[\frac{k_{hz}n_d}{k_{dz}n_h}+\frac{n_h}{n_d}\right]\exp(-i(k_{hz}-k_{dz})l_h) \end{pmatrix}$$

$$[F]=\begin{pmatrix} \frac{1}{2}\left[\frac{k_{dz}n_h}{k_{hz}n_d}+\frac{n_d}{n_h}\right]\exp(ik_{dz}(l_h+l_d)) & \frac{1}{2}\left[\frac{k_{dz}n_h}{k_{hz}n_d}-\frac{n_d}{n_h}\right]\exp(-ik_{dz}(l_h+l_d)) \\ \frac{1}{2}\left[\frac{k_{dz}n_h}{k_{hz}n_d}-\frac{n_d}{n_h}\right]\exp(ik_{dz}(l_h+l_d)) & \frac{1}{2}\left[\frac{k_{dz}n_h}{k_{hz}n_d}+\frac{n_d}{n_h}\right]\exp(-ik_{dz}(l_h+l_d)) \end{pmatrix}$$

The subindex *o* stands for the incident medium, the subindex *h* corresponds to the layer with high refractive index in the periodic strucure, the subindex *d* refers to the defect and the subindex *t* stands for the transmitted medium in the given expressions.

The matrix [T'] appearing in the same page is identical to [T], since both periodic structures constituting the truncated 1D photonic crystal of chapter 2 are identical and the choices in the phases of each component electric field at the layers forming the second periodic structure have been choosen conveniently in order to be independent of their position in the structure. The number of layers in each structure N and N' is also supposed identical.

References

[Abr79] E. Abrahams, P.W. Anderson, D.C. Licciardello, and T. Ramarkrishnan. Phys.Rev.Lett. **42**, 673-676 (1979).

[Alb85] M.P. Van Albada and A. Lagendijk. Phys.Rev.Lett. **55**, 2692-95 (1985).

[And58] P.W. Anderson, Phys.Rev. 109, 1492-1505. (1958).

[Arm62] J.A. Armstrong, N. Bloembergen, J. Ducuing and P.S. Pershan. Phys.Rev.**127**, 713 (1962).

[Ash82] N.W. Ashcroft and N. D. Mermin *Solid State Physics* (Holt, Rhinehart&Winston Inc., New York 1976).

[Ayr86] K. Ayra, Z.B. Su and J.L. Birman. Phys.Rev.Lett. **57**, 2725-2729 (1986).

[Ben96] J.M. Bendickson, J.P. Dowling and M. Scalora. Phys.Rev.E, **53**, 4107-4121 (1996).

[Ber97] V. Berger. J.Opt.Soc.Am.B. **14,** 1351 (1997).

[Beth89] D.S.Bethune. J.Opt.Soc.Am.B. **6**, 910-916. (1989).

[Bloe] N. Bloembergen. *Nonlinear optics.*(Benjamin. New York, 1965).

[Blo62] N. Bloembergen and S. Pershan. Phys.Rev. **128**, 606-622. (1962).

[Blo68] N. Bloembergen, R.K. Chang, S.S. Jha and C.H. Lee, Phys.Rev.**174,** 813 (1968).

[Blo70] N. Bloembergen and A. J. Sievers, Appl.Phys.Lett. **17**, 483-485 (1970).

[Bow93] C.M. Bowden, J.P. Dowling and H.O. Everitt. *Development and applications of materials exhibiting photonic band gaps.*J.Opt.Soc.Am.B, **10,** 280-413 (1993).

[Boyd] Boyd. *Nonlinear Optics.* ( )

[Bro69] F. Brown and M. Matsuoka. Phys.Rev. **185**, 985 (1969).

[Bur97] S.E. Burns, N. Pfeffer, J. Grüner, M. Remmers, T. Javoreck, D. Neher and R.H. Friend. Adv. Matt. **9**, 395 (1997).

[Car84] R.J. Carlsson and S.A. Asher. Appl.Spectrosc. **38**, 297 (1984).

[Che73] J.M. Chen, J.R. Bower, C.S. Wang and C.H. Lee, Opt.Comm. **9**, 132 (1973).

[Che81] C.K. Chen, T.F. Heinz, D. Ricard and Y.R. Shen, Chem.Phys.Lett. **83**, 455 (1981).

[Che95] C. Cheng and A. Scherer. J.Vac.Sci.Technol. B **13**, 2696-2700 (1995).

[Coj99] C. Cojocaru, J. Martorell, R. Vilaseca, J. Trull and E. Fazio. Appl.Phys.Lett.**74**, 504-506 (1999).

[Dick85] B. Dick, A. Gierulski and G. Marowsky. Apl.Phys.B **38**,107-116 (1985).

[Dob] J.A. Dobrowolsky. *Coatings and Filters.*

[Dow92] J.P. Dowling and C.M. Bowden. Phys.Rev.A. **46**, 612 (1992).

[Dow94] J.P. Dowling, M. Scalora, M.J. Bloemer and C.M. Bowden. J.Appl.Phys. **75**,1896-1899 (1994).

[Dre70] K.H. Drexhage, Sci.Am. **222**, 108 (1970).

[Dul78] A. Dulic and C. Flytzanis. Opt.Comm. **25**, 402 (1978).

[Eck84] R.C. Eckardt and J. Reintjes. IEEE J.Quantum.Electron.**QE-20**, 1178-1187 (1984).

[Eco89] Phys.Rev.B. **40**, 1334-1337 (1989).

[Ete86] S. Etemad, R. Thompson and M.J. Andrejco. Phys.Rev.Lett. **57**, 575-579 (1986).

[Fan94] S. Fan, P. Villeneuve, R. Meade and J. Joannopoulos. Appl.Phys.Lett.**65**, 1466-1468 (1994).

[Fej92] M.M. Fejer, G.A. Magel, D.H. Jundt and R.L. Byer. IEEE J.Quantum.Electron.**28**, 2631-2654 (1992).

[Fer99] A. Ferrando, E. Silvestre, J.J. Miret, P. Andres and M.V. Andres. Opt.Lett. **24**, 276 (1999).

[Gar82] S. Garoff, R. Stephens, C.S. Hanson, E.K. Sorenson. Opt.Commun. **41**, 257 (1982).

[Gio62] J. A. Giordamine. Phys.Rev.Lett.**8**,19 (1962).

[Guo86] P. Guoy-Sionnest, W. Chen and Y.R. Shen. Phys.Rev.B.**33**, 8254 (1986).

[Has95] N. Hasizume, M. Oshashi, T. Kondo and R. Ito. J.Opt.Soc.Am.B. **12**, 1894 (1995).

[Hat97] T. Hatori, N. Tsurumachi and H. Nakatsuka. J.Opt.Soc.Am.B, **14**, 348 (1997).

[Hecht] Hecht, Zajac. *Optica.* (Addisson-Wesley) 1986.

[Hei82] T.F. Heinz, C.K. Chen, D. Ricard and Y.R. Shen. Phys.Rev.Lett. **48**, 478 (1982).

[Hei83] T.F. Heinz, H.W.K. Tom and Y.R. Shen. Phys.Rev.A.**28**, 1883 (1983).

[Heinz] T.F. Heinz, in *Nonlinear Surface Electromagnetic Phenomena*, H.E. Ponath and G.I. Stegeman, eds. (North-Holland, Amsterdam, 1991), Chap. 5.

[Hil69] P.A. Hiltner and I.M. Krieger. J.Chem.Phys. **73**, 2386 (1969).

[Ho90] K.M. Ho, C.T. Chan and C.M. Soukoulis. Phys.Rev. Lett. **65**, 3152-3155 (1990).

[Hol90] R. W. Hollering and W.J.O. Teesselink. Opt.Comm.**79**, 224 (1990).R.W.J. Hollering, Q.H.F. Vrehen and G. Marowsky. Opt.Comm, **78**, 387-392 (1990).

[Hui93] N.F.Johnson and P.M. Hui. Phys.Rev.B. **48**, 10118-10123 (1993).

[Jackson] See, for example, Jackson J D 1975 *Classical Electrodynamics* 2nd edn (New York:Wiley) Chapter 6.

[Jeos] JeosB. Quantum.Semiclass.Opt. *Special issue on* $\chi^{(2)}$ *second order nonlinear optics: from fundamentals to applications.* **9** (1997).

[Jha65] S.S. Jha, Phys.Rev. **140**, A2020 (1965); Phys.Rev.Lett. **15**, 412 (1965).

[Jha67] S.S. Jha and C.S. Warke, Phys.Rev.**153**, 751 (1967); **162**, 854 (1967).

[Joann] J.D. Joannopoulos, R.D. Meade and J.N. Winn. *Photonic crystals.*(Princeton University Press, 1995)

[John84] Sajeev John. Phys.Rev.Lett. **53**, 2169-2172 (1984)

[John87] Sajeev John. Phys.Rev.Lett. **58,** 2486-2489 (1987).

[John88] S. John and R. Rangarajan. Phys.Rev.B. **38,** 10101-10104 (1988).

[John90] S. John and J. Wang. Phys.Rev.Lett. 2418-2421 (1990).

[John91] Sajeev John. Physics Today.32-40 May 1991.

[Kau98] M. Kauranen, Y. Van Rompaey, J.J. Maki and A. Persoons. Phys.Rev.Lett. **80,** 952 (1998).

[Kni98] J.C. Knight, T.A. Birks, P.St.J. Russell an D.M. Atkin, Opt.Lett.**21,** 1547 (1996); **22,** 484 (1997).

[Koh83] M. Kohmoto and L.P. Kadanoff and C. Tang. Phys.Rev.Lett. **50,** 1870-73 (1983).

[Kra93] B. Kramer and A. MacKinnon.*Localization:theory and experiment.* Rep.Prog.Phys. **56,** 1469-1564 (1993).

[Kur94] G. Kurizki, J.W. Haus.*Special issue:Photonic band structures.*J.Mod.Opt. **41,** 171-404 (1994).

[Kwe95] Gyeong-il Kweon and N.M. Lawandy. Opt.Comm. **118,** 388-411 (1995).

[Law88] N.M. Lawandy, S.A. Johnston and J. Martorell. Opt.Comm.**65,** 425 (1988).

[Leod] Leod. *Thin Film Optics.*

[Leu90] K.M. Leung and Y.F. Liu. Phys.Rev.Lett. **65,** 2646-2649 (1990).

[Lid97] D.G. Lidzey, D.D.C. Bradley, M.A. Pate, J.R. David, T.A. Fisher and M.S. Skolnick, Appl.Phys.Lett, **71,** 744 (1997).

[Mak62] P.D. Maker, R.W. Terhune, N. Nisenoff and C. Savage. Phys.Rev.Lett.**8,**21 (1962).

[Mar90] Jordi Martorell and N.M.Lawandy. Phys.Rev.Lett. **65,** 1877-1880 (1990).

[Mar94] Jordi Martorell and R. Corbalán. Opt.Comm.**108,**319-323 (1994).

[Mar97] Jordi Martorell, R. Vilaseca and R. Corbalán. Appl.Phys.Lett.**70,**702-704 (1997).

[Mar97b] Jordi Martorell, R. Vilaseca and R. Corbalán. Phys.Rev.A. **55,** 4520-4525 (1997).

[Mas96] J. Massaneda, F. Flory, S. Bosch, J. Martorell and S. Monneret. Laser optics&Vision for productive manufacturing. Proc. Society Photo-Optical Instrumentation Engineering, 2782 "Optical inspection and micromeasurements" (1996).

[Mee90] S.R. Meech and K. Yoshihara. J.Phys.Chem. **94,** 4913-4920 (1990).

[Miz88] V. Mizrahi and J.E. Sipe. J.Opt.Soc.Am.B. **5,** 660 (1988).

[Özb94] E. Özbay et al. Appl.Phys.Lett. **64,** 2059-2061 (1994).

[Pla91] S.L. McCall and P.M. Platzman. Phys.Rev.Lett. **67,** 2017-2020 (1991).

[Pie83] P. Pieranski. Contemp.Phys. **24,** 25-73 (1983).

[Prasad] P.N. Prasad and D.J. Williams *Introduction to nonlinear optical effects in molecules and polymers.*(John Wiley & Sons. 1991).

[Ram95] Y. Van Rompaey, M. Kauranen, J.J. Maki and A. Persoons. Phys.Rev.A. **51,** R4349 (1995).

[Ros96] A. Rosenberg, R.J. Tonucci and E.A. Bolden. Appl.Phys.Lett. **69,** 2638-2640 (1996).

[Sat90] S. Satpathy, Z. Zhang and M.R. Salephour. Phys.Rev.Lett. **64**, 1239-1242 (1990).

[Sca94] M. Scalora, J.P. Dowling, C.M. Bowden and M.J. Bloemer. Phys.Rev.Lett **73**, 1368 (1994).

[Sca94b] M. Scalora, J.P. Dowling, C.M. Bowden and M.J. Bloemer. J.Appl.Phys. **76**, 2023 (1994).

[Sca95] M. Scalora, J.P. Dowling, A.S. Manka, C.M. Bowden and J.W. Haus. Phys.Rev.A. **52**, 726-734 (1995).

[Sca96] M. Scalora, R.J. Flynn, S.B. Reinhardt, R.L. Fork, M.J. Bloemer, M.D. Tocci, C.M. Bowden, H.S. Ledbetter, J.M. Bendickson, J.P. Dowling and R.P. Leavitt. Phys.Rev.E **54**, R1078-R1081 (1996).

[Sca97] M. Scalora, M.J. Bloemer, A.S. Manka, J.P. Dowling, C.M. Bowden, R. Viswanathan and J.W. Haus. Phys.Rev.A. **56**, 1 (1997).

[Shen] Y.R. Shen. *Principles of Nonlinear Optics.* (Wiley Intersicience. New York, 1984)

[Shen94] Y.R. Shen. Appl.Phys.A. **59**, 541-543 (1994).

[Sheng] Ping Sheng. *Scattering and localization of classical waves in random media.* World Scientific Series on Directions in Condensed Matter Physics-vol.8 (World Scientific, 1990).

[Sip87] J.E. Sipe. J.Opt.Soc.Am.B. **4**, 481 (1987).

[Smi93] D.R. Smith, R. Dalidaouch, N. Kroll, S. Schultz, S.L. McCall and P.M. Platzman. J.Opt.Soc.Am.B, **10**, 314 (1993).

[Spr86] R.J. Spry and D.J. Kosan. Appl.Spectrosc.**40**, 782 (1986).

[Ste96] G.I. Stegeman, D.J. Hagan and L. Torner. Opt.Quantum.Electr. **28**, 1691-1740 (1996)

[Sul97] Sullivan K G and Hall D G J.Opt.Soc.Am.B, **14**, 1160 (1997)

[Toc96] M.D. Tocci, M. Scalora, M.J. Bloemer, J.P. Dowling and C.M. Bowden. Phys.Rev.A, **53**,2799-2803 (1996).

[Tru95] J. Trull, R. Vilaseca, Jordi Martorell and R. Corbalán. Opt.Lett. **20**, 1746-48 (1995).

[Tru99] J. Trull, R. Vilaseca and Jordi Martorell. J.Opt.B: Quantum Semiclass.Opt.1, 307-314 (1999)

[Tru98] J. Trull, R. Vilaseca and Jordi Martorell. J.Opt.Soc.Am.B. **15**, 2581-2585 (1998).

[Wil74] R. Williams and R.S. Crandall. Phys.Rev.A. **48**, 225 (1974).

[Win98] J.N.Winn, Y. Fink, S. Fan and J. Joannopoulos. Opt.Lett. **23**, 1573-1575 (1998).

[Wolf85] Pierre-Etienne Wolf adn G. Maret. Phys.Rev.Lett. **55**, 2696-2699 (1985).

[Yab87] E. Yablonovitch. Phys.Rev.Lett. **58**, 2059-2062 (1987).

[Yab89] E.Yablonovitch and T.J. Gmitter, Phys.Rev.Lett. **63**, 1950-1953 (1989).

[Yab91] E. Yablonovitch, T.J. Gmitter, R.D. Meade, A.M. Rappe, K.D. Brommer and J.D. Joannopoulos. Phys.Rev.Lett. **67**, 3380 (1991).

[Yariv] Amnon Yariv and Pochi Yeh. *Optical wave propagation in crystals* (Wiley, New York). Chapter 6.

[Yarivb] Amnon Yariv. *Quantum Electronics*.(Wiley, New York 1989).

[Yar77] A. Yariv and P. Yeh. J.Opt.Soc.Am. **67**, 438 (1977).

[Yeh76] P. Yeh, A. Yariv and C.S. Hong, J.Opt.Soc.Am. **67**, 423-437 (1977).

[Zha90] Z. Zhang and S. Satpathy. Phys.Rev.Lett. **65**, 2650-2653 (1990).

[Zha95] Daozhong Zhang, Zhaolin Li, Wei Hu, Bingying Cheng, Appl.Phys.Lett.**67**, 2431 (1995).

[Zer] F. Zernike and J.E. Midwinter, *Applied Nonlinear Optics*, (Wiley, New York, 1973).

[Zie76] J.P. van der Ziel and M. Ilegems, Appl.Phys.Lett. **28**, 437 (1976)